

Study of Small Polaronic, Variable Hopping Conduction and Its Exploration By Impedance Analysis in I- Substituted $\text{CaCu}_3\text{Ti}_4\text{O}_{12}$ at O- Ion Site By Fine-Tuning The Electrical Properties, Grains and Grain Boundaries

Bhoomika Yadav

IIT Kanpur: Indian Institute of Technology Kanpur

Rajesh Kumar (✉ rajeshbhu1@gmail.com)

IIT Kanpur: Indian Institute of Technology Kanpur <https://orcid.org/0000-0001-7065-3259>

Kamal K. Kar

IIT Kanpur: Indian Institute of Technology Kanpur

Manas K. Ghorai

IIT Kanpur: Indian Institute of Technology Kanpur

Original Research

Keywords: Perovskite oxides, Dielectric properties, Impedance spectroscopy, Grain boundary

Posted Date: February 16th, 2021

DOI: <https://doi.org/10.21203/rs.3.rs-197861/v1>

License:   This work is licensed under a Creative Commons Attribution 4.0 International License.

[Read Full License](#)

Study of small polaronic, variable hopping conduction and its exploration by impedance analysis in I⁻ substituted CaCu₃Ti₄O₁₂ at O⁻ ion site by fine-tuning the electrical properties, grains and grain boundaries

Bhoomika Yadav^{a,b}, Rajesh Kumar^c, Kamal K. Kar^{a,c,*}, Manas K. Ghorai^d

^a Advanced Nanoengineering Materials Laboratory, Materials Science Programme, Indian Institute of Technology Kanpur, Kanpur 208016, India.

^b Chhatrapati Shahu Ji Maharaj University, Kanpur 208026, India.

^c Advanced Nanoengineering Materials Laboratory, Department of Mechanical Engineering, Indian Institute of Technology Kanpur, Kanpur 208016, India.

^d Department of Chemistry, Indian Institute of Technology Kanpur, Kanpur 208016, India.

***Corresponding Author**

Email: kamalkk@iitk.ac.in, Phone (+91) (512) 2597687, Fax: (+91) (512) 2597408.

Abstract

In this study, dielectric and impedance related investigation are carried out in solid-state synthesized iodine doped $\text{CaCu}_3\text{Ti}_4\text{O}_{12-x}\text{I}_x$ ($x= 0, 0.005, 0.05$ and 0.2) at anion site in the varying temperature (300-500 K) and frequency (20 Hz - 1 MHz). The detailed analysis of dielectric and scaled plot (Z'' , M'') confirm the Maxwell-Wagner relaxations unlike Debye type. Broad relaxation peaks in spectroscopic plots and nearly straight lines in admittance (Y'' vs. Y') and ϵ'' vs. ϵ' reveals the occurrence of various relaxation processes with a narrow distribution of time constants. Mismatch in peak frequencies of Z''/ Z''_{\max} and M''/ M''_{\max} suggest that relaxation mechanism is dominated by short-range (localized) movement of charge carriers. The twinning values of $E_a, \tau_{M''}$ (≈ 0.067 eV) and $E_a, \tau_{Z''}$ (≈ 0.081 eV) indicate the involvement of same type of charge carriers in conduction and relaxation processes. Correlating Jonscher's power law and overlapping peaks in the combined plot of M'' , Z'' vs. $\log f$ indicates high loss, due to DC conduction through localized hopping of small polarons via some defect states through Mott's VRH mechanism, among the highly concentrated density-of states, $N(E_f)$, confined in the very low-temperature zone and nearest-neighbor hopping (NNH) of polarons due to Arrhenius in high-temperature zone both reserved in low-frequency region (≤ 1 kHz) only.

Keywords: Perovskite oxides, Dielectric properties, Impedance spectroscopy, Grain boundary.

1. Introduction

Ceramics materials are inorganic non-metallic solid oxides, silicide nitrides, and carbides. Nowadays, electroceramics shows technological importance in actuators, sensors, capacitors, memory devices, electrically controlled microwave tuning devices for radar, etc. Oxide materials with an exceptionally high dielectric constant are in demand in the era of miniaturization with a potential role in microelectronic devices and high-density storage applications as capacitors and memory devices. TiO_2 and ATiO_3 based oxides (where, $\text{A}=\text{Ba}$, Ca , and Sr) lose small amount of oxygen and become conducting via hopping mechanism on firing in reducing atmosphere.[1] Limited re-oxidation can produce a thin insulating layer on the outer surfaces of pellets or along grain boundaries and outer regions of individual grains making them devices, which are known as surface barrier layer capacitor (SBLC) and internal barrier layer capacitor (IBLC) having high values of permittivity ≈ 10000 - 50000 that rely on the processing conditions.[1] Most commercial IBLC's are based on $(\text{Ba}, \text{Sr}, \text{Pb}) \text{TiO}_3$ ceramics, which requires complex multistage processing conditions i.e., high temperature, reducing atmosphere, and limited diffusion of oxygen along the grain boundary. These are the foundation stones of the capacitor industry. $\text{CaCu}_3\text{Ti}_4\text{O}_{12}$ has cornered $(\text{Ba}, \text{Sr}, \text{Pb}) \text{TiO}_3$ based IBLC's. Subramanian et al. have reported $\text{CaCu}_3\text{Ti}_4\text{O}_{12}$ of $\text{ACu}_3\text{Ti}_4\text{O}_{12}$ family ($\text{A}=\text{Ca}$, Sr , Ba , $\text{Bi}_{2/3}$, $\text{Y}_{2/3}$, and $\text{La}_{2/3}$).[2] These are oxides having pseudo-cubic perovskite structure, space group $\text{Im}\bar{3}$ (No.204) with a lattice parameter of 7.391 \AA . [2] $\text{CaCu}_3\text{Ti}_4\text{O}_{12}$ has Ca at corner and body center position and Cu at face center and mid of edges. The size difference of Ca^{+2} and Cu^{+2} causes tilting of TiO_6 octahedra (tilt angle being 141° and Ti occupies the centrosymmetric position within the octahedra) giving square planar environment to Cu making calcium copper titanate (CCTO) a rigid structure. Ca-O distance is 2.604 \AA , which is much less than 2.72 \AA , the value is predicted, based on the ionic radii.[2] So Ca is in a site too small for it and it pushes out to expand the lattice. Thus places the Ti-O bond under tension and increases the polarizability of TiO_6 octahedra.[2] So $\text{CaCu}_3\text{Ti}_4\text{O}_{12}$ has exceptionally high ($\epsilon_r \approx 10^5$ for single crystal and 10^4 for bulk) permittivity almost independent of temperature and frequency.[3] This makes it eye-catching for device application. Due to the low site symmetry of Ti^{+4} in CCTO than in BaTiO_3 , an idea of local dipole moments, associated with off-centre displacement of Ti^{+4} ions may be the reason for high permittivity came up, but the transition to the ferroelectric state is obstructed by tilting of TiO_6 octahedra to accommodate the square planar coordination of Cu^{+2} . [2] Also ϵ_r in CCTO drops to ≈ 100 below 150 K without any structural phase transition as powder neutron diffraction data showed the structure remains cubic and centrosymmetric for less than 35

K.[1] Homes *et al.*[2] reported the idea of freezing (relaxing out) of local dipole moments, a satisfactory note on the decrease in permittivity below 150 K, but Subramaniam *et al.*[2] suggested that many isostructural compounds contains lower room temperature permittivity values ($\epsilon_r \approx 409$ for $\text{CdCu}_3\text{Ti}_4\text{O}_{12}$ and $\epsilon_r \approx 33$ for $\text{YCu}_3\text{Ti}_3\text{FeO}_{12}$). To date, IBLC based on electrical heterogeneous microstructure (with electrically insulating grain boundary surrounded by semiconducting grains thereby forming the enormous micro capacitors) is the most accredited theory to explain colossal dielectric constant in CCTO and high concentrations of twinning and planar defects as an alternative of the barrier layer in single crystal.[1] CCTO has cornered BaTiO_3 based perovskites, whose high dielectric constant, $\epsilon_r \approx 1000$ is temperature-dependent and shows a drastic decrease at curie temperature (detrimental for device application) and also Pb based toxic relaxor ferroelectrics as $\text{PbMn}_{1/3}\text{Nb}_{2/3}\text{O}_3$, characterized by ferroelectric response under high electric field at a lower temperature but no-macroscopic spontaneous polarization.[4] To commercialize CCTO as a capacitive element in energy storage devices high dielectric constant and low loss is the key factor. High loss in CCTO restricts its commercial use as ceramic capacitors.[3,4] CCTO has budding applications in curtailing the size of capacitors, actuators, sensors variable resistors, etc. Recently novel nanocomposites of silica-coated calcium copper titanate-graphene ($\text{CCTO@SiO}_2\text{-GO}$) and ($\text{CCTO@SiO}_2\text{-NH}_2$) has been synthesized which can be used in designing new functional electronic devices and electrochemistry.[5,6]

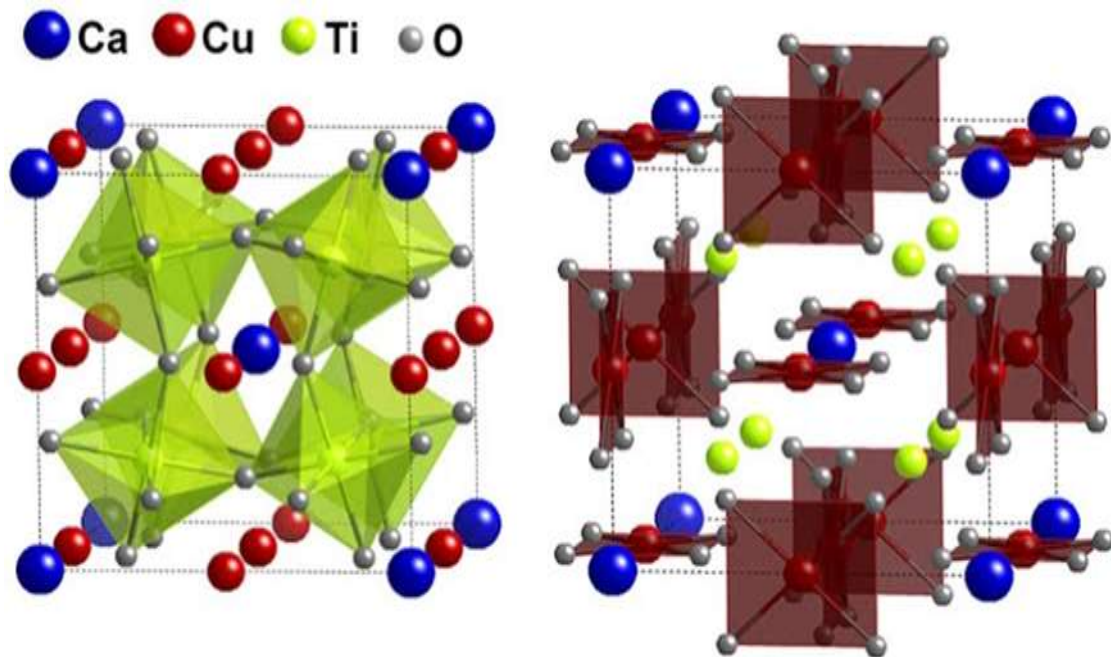


Fig. 1. Schematic representation of crystalline structure of $\text{CaCu}_3\text{Ti}_4\text{O}_{12}$.

The electrical properties of $\text{CaCu}_3\text{Ti}_4\text{O}_{12}$ are likely to depend on many variables like ceramic microstructure (average grain size, porosity, and pellet density) and processing conditions (sintering temperature, time, cooling rate, oxygen partial pressure while sintering, etc.).[7] Till date effect of very large variety of substitutions (aliovalent, isovalent, heterovalent, etc.) have been reported like Fe^{+2} , [7], Ba^{+2} , [8], Sr^{+3} , [9], Ag^1 , [10], Eu^{+2} , [11], La^{+3} , Ni^{+2} , [12], Mg^{+2} , [13], Zn^{+2} , Ga^{+3} , Zr^{+4} , Sn^{+2} , [14], Nb^{+5} , Ta^{+5} , [15], rare earth[16], Ta^{+5} , [15], Sn^{+2} , [14], La^{+2} , [17] and Zn^{+2} , [17] co-doping and many more at Ca^{+2} , Cu^{+2} , Ti^{+4} sites into CCTO affecting the values of ϵ , $\tan \delta$, grain resistance (R_g), grain boundary resistance (R_{gb}), activation energy of grain (E_{ag}), activation energy of grain boundary (E_{agb}), etc. to improve the electrical properties (increase permittivity and lower the loss value). Substitution of higher cations say Ta^{+5} or Nb^{+5} at Ca^{+2} , Cu^{+2} or Ti^{+4} site will increase the charge inside the grain, reducing R_g and thereby increase the space charge polarization, which will increase the permittivity, ϵ , but will also increase the loss value by decreasing R_{gb} due to the leaky grain boundary. Alternatively, doping Mg^{+2} , Sn^{+2} , etc. will reduce $\tan \delta$, but simultaneously reduces permittivity value by reducing charge carrier within the grain.[14] Also, the grain boundary can be made less leaky (i.e., high R_{gb}) by decreasing the oxygen vacancy to depress conduction via hopping. The most accepted model to explain this behavior is IBLC/ SBLC based, which is debatable to date concerning its origin. Due to electrically heterogeneous microstructure, CCTO exhibits non-ohmic property. This is due to the existence of back to back electrostatic barrier (Schottky barrier), which is confirmed by Kelvin Probe Force Microscopy.[18] The nonlinear coefficient, $\alpha \approx 912$ for pure CCTO is greater than ZnO, a varistor material for which $\alpha \approx 30-80$, and is dependent upon microstructure.[18] So CCTO is an excellent candidate for varactor devices due to large α and it can be used as a surge protector when connected parallel to electronic devices.[18]

Study of impedance spectroscopy shows that high permittivity is due to IBLC's and SBLCs, which are surprisingly prepared by single-stage processing in the air at high temperature via limited re-oxidation to form a thin insulating layer at the surface and along grain-boundaries in CCTOs thus avoiding the trendy complex, multistage processing route required to manufacture IBLC's as in perovskites (say BaTiO_3 , SrTiO_3 , etc.) is the most important, applicative, and appealing part of CCTO.

In the present work, anion (oxygen) was partially replaced by iodine (different type of anion) in $\text{CaCu}_3\text{Ti}_4\text{O}_{12-x}\text{I}_x$ ($x = 0, 0.005, 0.05$ and 0.2) with the following motives. (1) Iodine substitution due to large ionic radii will enhance ionic (due to Jahn-Teller distortions in TiO_6

octahedra) and electronic ($\alpha_e=4\pi\epsilon_0r$, due to high radius of iodine) polarizability, thereby instantaneous saturation polarization without contributing any loss in the measured frequency and temperature range. (2) I_O site will increase the charge carriers within the grain due to charge compensation by reduction of valence states of Ti^4 to Ti^3 and Cu^2 to Cu^1 will reduce R_g thereby increase dielectric constant via space charge polarization within the grain.[13] (3) Another strategy followed was to reduce oxygen vacancy at the grain boundary by sintering in an oxygen atmosphere, which will reduce low-frequency loss by increasing R_{gb} . [19] Here doping with I ion makes no effect on insulating properties of grain boundaries as oxygen vacancies are filled during the cooling step of sintering process thus R_{gb} is increased and low-frequency loss is reduced due to decrease in dc conduction.[13] [19] Promotion of grain growth as I doping assist in liquid phase sintering and promoting the diffusion of ions along grain boundary while sintering will enhance permittivity. So, taking benefits of atomic structure apart from microstructure and thus enhancing permittivity in the high-frequency zone without the exertion of reducing loss in the low-frequency zone will heighten its commercial application is the novelty of this work.

2. Experimental and instrumentation

$CaCu_3Ti_4O_{12-x}I_x$ ($x= 0, 0.005, 0.05$ and 0.2) were synthesized by solid-state diffusion method using $CaCO_3$, CuO , TiO_2 , and AgI_2 (all analytical grade) with purity $\geq 96\%$ as raw materials. Stoichiometric amount of these were weighed and ball-milled in agate jar using agate balls as grinding media and ethanol as mixing media for 48 hours. After mixed powders were dried overnight, they were calcined for 12 hours at $1000\text{ }^\circ\text{C}$ to remove volatile impurities and were further mixed with 2% PVA. Finally, they were pressed into pellets at an optimized pressure of 250 MPa and kept in a programmed furnace at the rate of $5\text{ }^\circ\text{C min}^{-1}$ for three hours at $1000\text{ }^\circ\text{C}$ on hold to burn off the binder. Then the mixture was sintered at $1050\text{ }^\circ\text{C}$ for 15 hours later annealed through furnace cooling. XRD exposed crystal structure and phase analysis were done via X-Pert Hi score plus software package by PANalytical. For microstructural studies, the sintered pellets were polished using emery papers of various grades followed by velvet cloth polishing using alumina powder of $1\text{ }\mu\text{m}$ followed by diamond paste of $0.25\text{ }\mu\text{m}$ till mirror finished, then sonicated several times using distilled water to remove leftover particles of alumina, SiC, and diamond paste and finally were thermally etched at $1000\text{ }^\circ\text{C}$ for 15 mins to reveal the grain and grain boundary. Thermally etched samples were coated with Cu (by Cu sputtering) and observed under tungsten scanning electron microscopy (WSEM) attached with energy dispersive spectroscopy (EDS) for micro compositional analysis

to expose the ceramic microstructure. The surface morphology of sintered thermally etched ceramics was characterized using W-SEM. Elemental distribution of the dopant major elements in the sintered ceramics were examined using EDS. Dielectric measurements of Au pasted (to make electrical contacts) samples were done in the temperature of 300–450 K and frequency of 20 Hz to 1 MHz using (Agilent-LCR meter).

3. Results and discussion

3.1. Phase composition and crystal structure

The phase purity and crystallinity of compositions ($\text{CaCu}_3\text{Ti}_4\text{O}_{12-x}\text{I}_x$, where $x=0, 0.2, 0.05,$ and 0.005) were examined by XRD (Figs. 2a, 2b, 2c, 2d and S1).

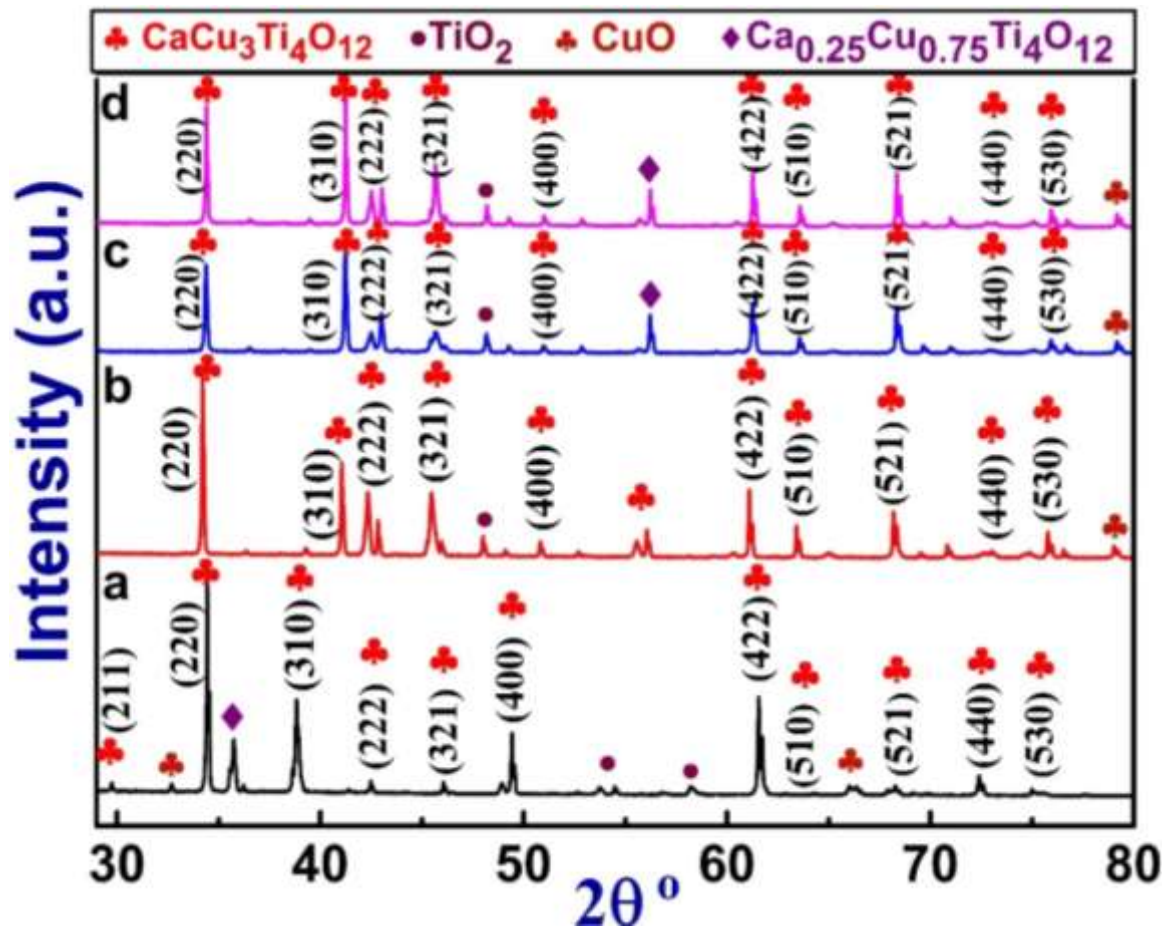


Fig. 2. XRD pattern of (a) $\text{CaCu}_3\text{Ti}_4\text{O}_{12}$, (b) $\text{CaCu}_3\text{Ti}_4\text{O}_{11.995}\text{I}_{0.005}$, (c) $\text{CaCu}_3\text{Ti}_4\text{O}_{11.95}\text{I}_{0.05}$, and (d) $\text{CaCu}_3\text{Ti}_4\text{O}_{11.8}\text{I}_{0.2}$.

The phase analysis was done using X-pert Hi score plus. The diffraction peaks of all compositions were indexed on the basis of (JCPDS File No.-75-2188). Formation of a major phase of parent material, $\text{CaCu}_3\text{Ti}_4\text{O}_{12}$ along with few traces of secondary phases as TiO_2 , (JCPDS-01-088-1173), CuO , (JCPDS-00-001-1117), $\text{Ca}_{0.25}\text{Cu}_{0.75}\text{Ti}_3\text{O}_3$, (JCPDS-00-021-0140), etc. were noticed in all compositions. This may be due to the low diffusivity of iodine

through nano-sized grains at oxygen site. To ensure the changes in crystal structure of the CCTO ceramics lattice parameter of $\text{CaCu}_3\text{Ti}_4\text{O}_{12-x}\text{I}_x$ ($x= 0, 0.005, 0.05$ and 0.2) was calculated using equation $a = d\sqrt{h^2 + k^2 + l^2}$. Small deviation in lattice parameter from the standard value (7.391 \AA) for all compositions were noticed as shown in table 1. This, may be i). due to differences in the ionic radius of the host oxygen anion (0.152 nm) and substituent iodine anion (0.22 nm) or, ii) due to the presence of Ti^4 as Ti^3 leading to Jahn–Teller distortions in TiO_6 octahedra.[20] In zoomed view of (220) peak (Fig. S1) shows the shifting of (220) peak at 34° towards low angle side for all compositions indicating a change in lattice parameter due to lattice distortions owing to compressive residual stress of crystal structures.[13]

Table 1. Tabulated value of grain size, lattice parameter, crystallinity, and particle size.

Com position, x	Grain size (\AA) (XRD), Scherer formula.	Lattice parameter, \AA (XRD)	Crystallinity (XRD) % \approx	Dislocation density $\times 10^{-3}$ (XRD)	Micro strain $\times 10^{-3}$ (W-H plot)	Grain size W-H plot (\AA)	Particle size (μm) SEM
0	533	7.481	77	0.3	4	119	2.3
0.005	440	7.563	95	0.5	3	400	2.2
0.05	632	7.620	95	0.2	0.3	434	2.3
0.2	836	7.659	95	0.1	1	369	2.5

Grain size/crystallite size, D for the bulk pellet was calculated using Scherer equation, $D = K\lambda/\beta\cos\theta$, where $K=0.9$ or 1 is the structure factor, λ =wavelength of Cu-K α radiation (1.54 \AA), β is the FWHM (full-width half maxima) in radians and is given by $\beta=\sqrt{(\beta^o - \beta^i)}$, where β^o is the width observed from the XRD peak, β^i is the width due to instrumental effects and θ is the peak position value in radians. Peak gets broader as the grain size gets smaller (Fig. S1) justifying Scherer formula as FWHM is inversely proportional to grain size (i.e. $\beta \propto 1/D$). Other contributions to peak broadening are faulting, solid solution inhomogeneity, temperature factors, etc.

Since crystallite size and strain value vary as a function of 2θ , so Williamson- Hall plot is used to determine crystallite size and microstrain as shown in table 1. Microstrain is contributed due to the non-uniform lattice distortions, dislocations, antiphase domain boundaries, grain surface relaxation, etc.

Density and porosity measurement were calculated through Archimedes' principle using equations S1 and S2 (supplementary information). Theoretical density was calculated from the lattice parameter and molecular weight of the sample. Some pores were observed at the triple points at grain boundaries (Fig. 3). Porosity decreases with increasing the value of x and it reveals that iodine improves densification.

3.2. Microstructure characterization

SEM images in Fig. 3 shows the typical micrographs of cuboid, and elongated rectangular-shaped morphologies with particle size in range of 1 to 7 μ m. Segregation of Cu at grain boundary along with few secondary phases were confirmed via EDS analysis. Cu segregation led to the formation of the liquid phase at grain boundaries which assisted diffusion leading to grain growth.[13] As reported large grain size enhances the dielectric constants.[21] In this report largest grain size was noticed for $\text{CaCu}_3\text{Ti}_4\text{O}_{11.8}\text{I}_{0.2}$ (Fig. 3d). This lead to enhancement in dielectric constant from $\approx 1 \times 10^3$ (undoped: $\text{CaCu}_3\text{Ti}_4\text{O}_{12}$, Fig. 4a) to $\approx 1 \times 10^4$ for doped composition ($\text{CaCu}_3\text{Ti}_4\text{O}_{11.8}\text{I}_{0.2}$; Fig. 5a) and it has also explained in accordance with equation (1) in the dielectric analysis of CCTO.

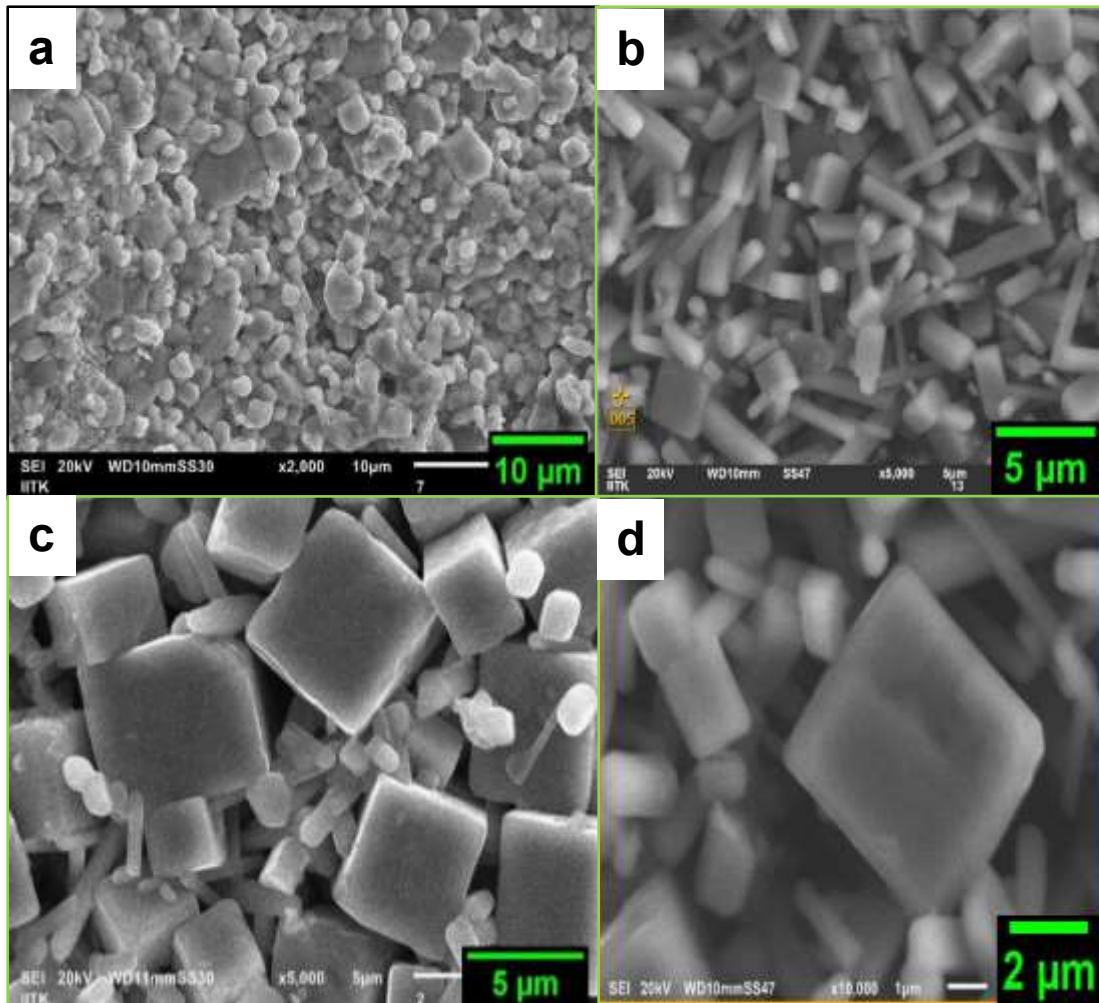


Fig. 3. SEM images of (a) $\text{CaCu}_3\text{Ti}_4\text{O}_{12}$, (b) $\text{CaCu}_3\text{Ti}_4\text{O}_{11.995}\text{I}_{0.005}$, (c) $\text{CaCu}_3\text{Ti}_4\text{O}_{11.95}\text{I}_{0.05}$ and (d) $\text{CaCu}_3\text{Ti}_4\text{O}_{11.8}\text{I}_{0.2}$

3.3. Dielectric analysis

Typical plots of dielectric constant, ϵ_r and $\tan \delta$ vs. temperature for $x=0$ and 0.2 are shown in Figs. 4a, 4b and Figs. 5a, 5b respectively. ϵ_r and $\tan \delta$ vs. log frequency plots for the compositions with $x=0$ and $x=0.2$ are shown in Figs. 4c, 4d and Figs 5c, 5d respectively. Proportional relation of dielectric constant and loss with temperature were noticed for all compositions.

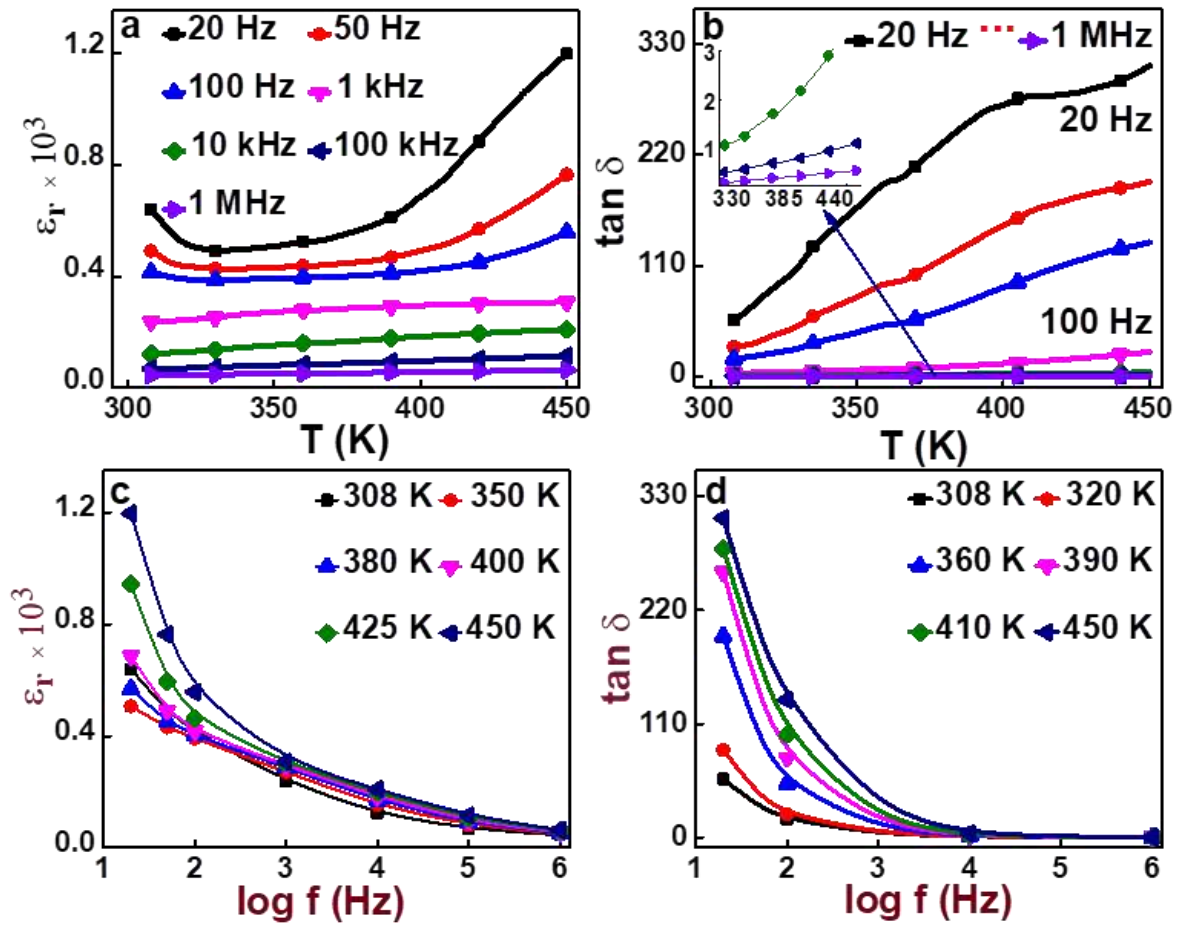


Fig. 4. Variation of (a) ϵ_r and (b) $\tan \delta$ with temperature at 20 Hz, 50 Hz, 100 Hz, 1 kHz, 10 kHz, 100 kHz and 1 MHz and (c) ϵ_r and (d) $\tan \delta$ with log frequency at few steady temperatures for the composition, $\text{CaCu}_3\text{Ti}_4\text{O}_{12}$

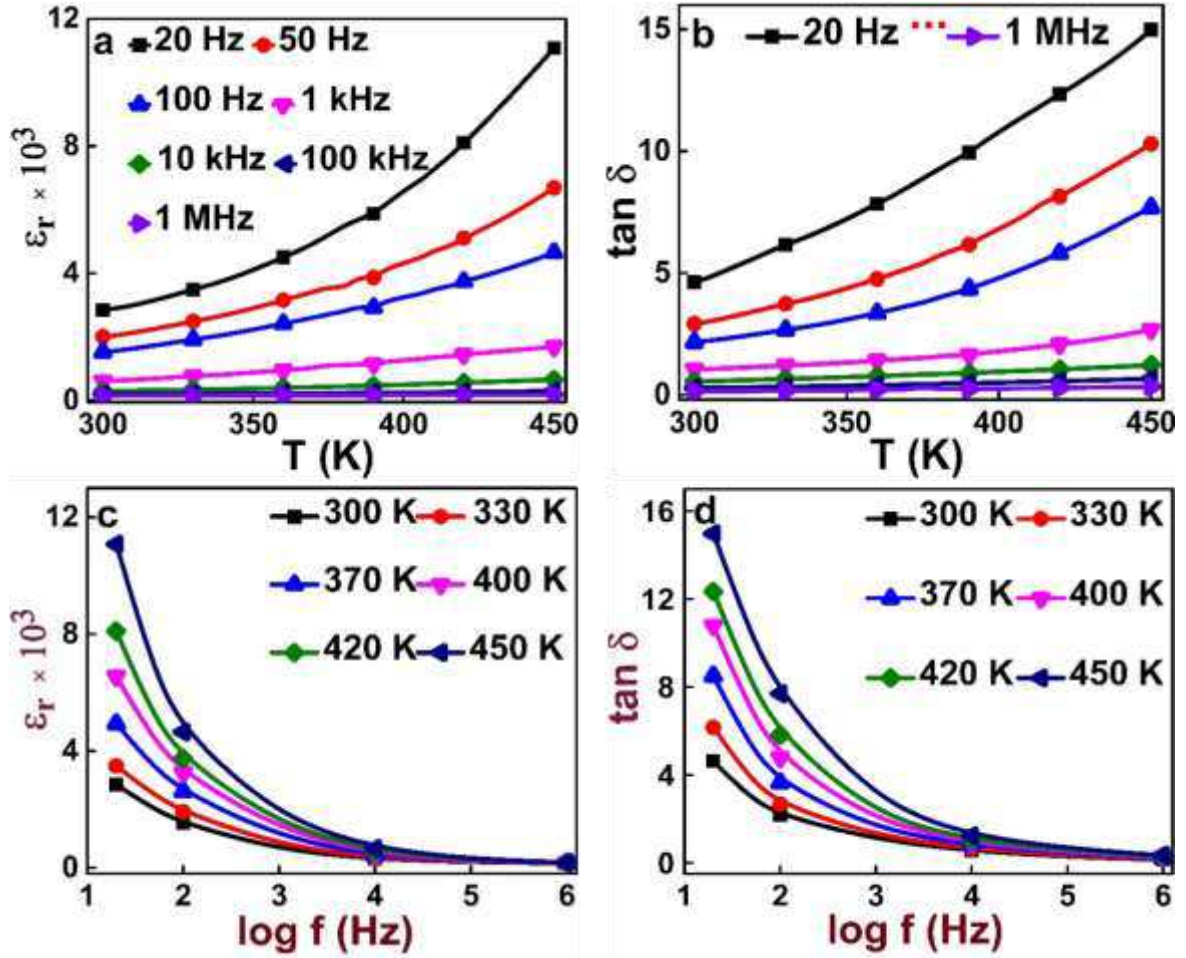


Fig. 5. Variation of (a) ϵ_r and (b) $\tan \delta$ with temperature at 20 Hz, 50 Hz, 100 Hz, 1 kHz, 10 kHz, 100 kHz and 1 MHz and (c) ϵ_r and (d) $\tan \delta$ with log frequency at few steady temperatures for the composition, $\text{CaCu}_3\text{Ti}_4\text{O}_{11.8}\text{I}_{0.2}$.

Maximum dielectric constant ($\approx 2.97-0.29$) $\times 10^3$ and minimum loss ($\approx 0.1-0.2$) occurred for $\text{CaCu}_3\text{Ti}_4\text{O}_{11.8}\text{I}_{0.2}$ for almost entire temperature and frequency range (Table S2). In this case dielectric constant increased by 10 decades and loss decreased by 100 order at 20 Hz (Figs. 5a, 5b). This can be attributed to large grain size and formation of IBLC's. If it is assumed that, grain and grain boundary form a two-layer capacitor with a thickness ($d_g + d_{gb}$), where d_g and d_{gb} are thicknesses of grain and grain-boundary layer respectively. The effective dielectric constant for IBLC's is given by, $\epsilon'_s = \epsilon_{gb} \left(\frac{d_g + d_{gb}}{d_{gb}} \right)$ -----(1), (where ϵ_{gb} is the dielectric constant of the grain boundary layer, which even low, will give large, ϵ'_s for large ratio, $\left(\frac{d_g + d_{gb}}{d_{gb}} \right)$, clearly showing its dependency on microstructure and hence maximum permittivity for large grains.[22]

Prominent mechanisms that lead to enhanced dielectric constants are ferroelectricity, charge-density wave (CDW) formation, hopping charge transport, the metal-insulator transition, and various kinds of interface effects.[23] Hopping conduction is the typical charge transport process of localized charge carriers. In electronic conductors, electrons/holes can localize due to disorder. In amorphous structure, the disorder may be due to doping (substitutional disorder) whereas in pure crystals it is due to slight deviations from stoichiometry or lattice imperfections.[23] The dielectric behavior can be judged in three regions.

Very low-frequency region, (20-100 Hz), $\omega \ll 1/\tau$ It was found that for all compositions, ϵ_r and $\tan \delta$ exhibits increase from almost plateau region (Figs. 4a, 4b, 5a, 5b, S2a, S2b, S3a and S3b) at low temperature to high value followed by a sharp and rapid rise from adjacent another plateau to exceptionally high value, $\epsilon_r \approx 10^3$ for 20 kHz at ≈ 450 . This may be due to SBLC effect at the sample-electrode interface. Since dipoles follow the field for $\omega \ll 1/\tau$, where τ is the relaxation time, giving rise to space charge polarization/dipolar polarization (via segregation of ions, their difference in conductivities[7]/depletion layer of Schottky barrier, etc. or non-stoichiometric surface/oxygen deficiency/heterogeneities due to environment oxidation or defects/secondary phases etc.). The transition temperature between two plateau regions shifts to a higher temperature side with increasing frequency analogous to relaxors.[7] Here in this case for all compositions, (Figs. 4a, 5a, S2a, S3a), the inflection in ϵ_r with T is accompanied by loss peak in $\tan \delta$ vs. T plot, as shown in Figs. 4b, 5b, S2b, S3b, which shifts exponentially to a higher frequency with temperature seems to be characteristics of Debye-type dipolar relaxation with thermally activated relaxation rate.[24][25]. This behaviour hints CCTO to be of non-ferroelectric nature due to absence of ferroelectric phase transition. But at the same time as the inflection point in ϵ_r vs. T and loss peak in $\tan \delta$ vs. T are not at the same temperature (so Debye-type relaxation too is ruled out). Speculating now that CDC behavior may be due to the Maxwell-Wagner type extrinsic effect. At interfaces (metal to insulator contacts, intergrain boundaries) depletion layers are formed due to the formation of Schottky barriers forming BLC's yielding Maxwell-Wagner type relaxations. In general, if the work function of the metal electrode is higher than of electron semiconductor, then in the contact region of the semiconductor the electron concentration is curbed and a depletion layer appears which may lead to capacitive surface, forming BLC's giving rise to Maxwell-Wagner effect, which is also confirmed from humpy, semicircular arcs of Z'' vs. Z' , (Fig. 8a).[26]

Now further increasing frequency but still in low-frequency zone ≤ 100 Hz due to inertial effect/ randomization, heavy ions/dipoles begin to lag behind the field rapidly decreasing the permittivity and enhancing the loss with increasing temperature. Furthermore by and large electronic polarization (10^{14} - 10^{15}) Hz, which is shifting of electron cloud with respect to nucleus, and ionic polarization (10^{10} - 10^{13}) Hz independent of temperature give rise to instantaneous saturation polarization. This do not make any contribution to loss due to their high frequency operating range in the measured frequency 20 Hz to 1 MHz and temperature 300-450 K. This clarifies reason for loss in all compositions as shown in Figs. 4d, 5d, S2d, S3d.

Mid-frequency region, (100 Hz-1 kHz), $\omega < 1/\tau$ Owing to IBLC effect at grain boundaries (due to segregation of defects/ions or depletion region, porosity, grooves, Cu segregation, etc.) leads to dipolar polarization and enhances the dielectric constant but of lower magnitude and due to inertia and its randomization with temperature rise, the loss gets enhanced.[27] Correlating this with electrical microstructure as shown in Fig. 15d, (for $\text{CaCu}_3\text{Ti}_4\text{O}_{11.995}\text{I}_{0.005}$), increase of C_g with temperature, increases the polarization within the capacitive layer (grain) due to which permittivity gets enhanced with temperature rise which clearly explains the increase of ϵ_r with temperature as shown in Figs. 4a, 4c, 5a, 5c, S2a, S2c, S3a, S3c, and decrease of R_{gb} (for $\text{CaCu}_3\text{Ti}_4\text{O}_{11.995}\text{I}_{0.005}$), (Fig.15a) leads to increase of loss with temperature rise (Figs. 4b, 4d, 5b, 5d, S2b, S2d, S3b. S3d), thus it's R_{gb} and C_g which mostly governs the mid-frequency permittivity and loss.

Very high-frequency region, (1 kHz -1 MHz), $\omega \gg 1/\tau$ dipoles, space charge do not follow such high-frequency field and won't respond at all so, $\epsilon_r = \epsilon_\infty \leq 10^2$ is mostly due to instantaneous saturation polarization via electronic and ionic polarization, which remains almost independent of entire frequency and temperature range. So successively lowest magnitude ϵ_r and $\tan \delta$ almost dormant with temperature were noticed. The underlying physics using Jonscher's power law revealed that it's the small polaron hopping/lagging within the grain, the reason for permittivity/loss as clarified in ac conductivity study.

By the way, high loss lowers CCTO's marketing zone. A profound study has to be done to resolve this issue. The dielectric loss of dielectric material results from (1) distortional (related to electronic and ionic polarization which is negligible due to their very high resonance frequencies), (2) interfacial (movement or rotation of atom or molecules in an ac field) and (3) conduction loss attributed to dc electrical conductivity which represents the

actual flow of charge through materials or hopping mechanism via oxygen vacancy at grain boundary due to leaky grain boundary (i.e., low R_{gb}).

Loss in very low and mid-frequency zone The plateau in low frequency region shown in the M' vs. $\log f$ (Fig.13c) indicated negligible electrode polarization, also validated from the high value of $E_a \tau_{s-el} \approx 1.2$ eV as shown in Fig. 15c (concludes that SBLC effect too for loss is ruled out here). The overlapped peaks (very low-frequency zone) in the combined normalized plots (Fig. 14) for $\text{CaCu}_3\text{Ti}_4\text{O}_{12}$ and $\text{CaCu}_3\text{Ti}_4\text{O}_{11.995}\text{I}_{0.005}$ respectively of M''/M_{\max} and Z''/Z_{\max} vs. $\log \omega$ suggested the occurrence of long-range conduction giving loss, which is favored by Jonscher's (UDR) law. So, its dc conduction (due to very low activation energy say, $E_{a\omega Z''} \approx 0.081$ eV and $E_{a\omega M''} \approx 0.067$ eV for most probable jump frequency) via hopping of small polarons in low-frequency zone contributes loss which gets intensifies with temperature. The governing equation for loss in the IBLC model is $\tan \delta = \frac{1}{\omega C R_{gb}} + \omega C R_g$, --- (2), where C is the measured capacitance of the sample.[28] In the mid-frequency zone, if R_{gb} is high, then according to $\tan \delta = \frac{1}{\omega C R_{gb}}$, the loss will be minimal. In Z'' vs. Z' plot, (Fig. 8a) arc size decreases with increasing temperature inferring decrease of R_{gb} contributing mid-frequency loss justified from Figs. 4a, 5a, S2a, S3a robustly supporting the BLC mechanism explanation for high dielectric constant. Also, a decrease of R_{s-el} , R_{gb} , and R_g with temperature rise (Fig. 15a, shown for $\text{CaCu}_3\text{Ti}_4\text{O}_{0.995}\text{I}_{0.005}$) suppresses the BLC effect, therefore, permittivity decreases with T, so ultimately loss gets maximized in low-frequency zone with temperature rise due to dc conduction and due to incomplete reversal of ions/dipoles owing to their inertia upon ac field reversal.[29][4]

High-frequency Zone As $\tan \delta = \omega C R_g$, so in the high-frequency field, the feeble response of ions/charges within grain makes ϵ_r low, furthermore R_g decreases very rapidly with increasing temperature in the high-frequency zone (Fig. 8a.) so do the loss and both are, almost independent of temperature and frequency. In Figs. 4c, 5c, S2c, S3c, ϵ_r vs. $\log f$, dispersion of ϵ_r in the low-frequency region is seen. Generally, this behavior is found for electrically insulating materials i.e. dielectrics in which mechanism of conduction via hopping type is present.[30][31] With increasing frequency the degree of dispersion decreases and beyond kHz no dispersion was found, also confirmed from Figs. 4a, 5a, S2a, S3a, favoring the Jonscher's UDR power law, $(i\omega\tau)^\beta$ with a negative exponent ($\beta < 1$). This indicates hopping of small polarons, as β increases with T, (Fig. 6b) via defect states.[31] This was also supported also by overlapping peaks in M'' vs. $\log f$ (Fig. 13b and S8b) in the

frequency ≈ 1 MHz (evidence of long-range conduction in the high-frequency zone) for $\text{CaCu}_3\text{Ti}_4\text{O}_{12}$ and $\text{CaCu}_3\text{Ti}_4\text{O}_{0.995}\text{I}_{0.005}$ respectively. The core physics behind these are clarified using Jonscher's power law (UDR) in the coming section ac conductivity study.

3.4. Effect of AC field on dielectric properties (AC conductivity study)

AC electrical measurements are utilized in identifying the dominant conduction process within the grain and grain boundary in BLC's, based on the formation of enormous micro capacitors of grain as electrode and grain boundary as the dielectric in CCTO.[32] Conduction originates due to electrons, ions, and polarons (via. defect states). AC conductivity was calculated using $\sigma_{ac} = \omega \epsilon_0 \epsilon''$ --(3), $\epsilon^* = \epsilon' + \epsilon'' = \frac{1}{i\omega C_0 |Z|^2}$ -- (4) where ϵ'

(dispersion) and ϵ'' (dielectric loss factor/absorption in medium), $\epsilon' = \frac{Z''}{\omega C_0 |Z|^2}$ -- (4a) and

$\epsilon'' = \frac{Z'}{\omega C_0 |Z|^2}$ ---- (4b) and $C_0 = \frac{\epsilon_0 A}{d}$ --- (5), d =sample thickness, A is the area of the sample, ϵ_0

is the free space permittivity. Real ac conductivity, $\sigma_{total} = \sigma_1(T) + \sigma_2(\omega, T) = \sigma_{dc} + \sigma_{ac} = \sigma_{dc} + A(i\omega\tau)^\beta$ ----- (6), the frequency dependence of conductivity is given by Jonscher's power

law which is a common feature of amorphous semiconductors and disordered systems.[33]·[34] Constant A , the strength of polarizability has a unit of conductivity, and β

(T, ω) is a dimensionless parameter, represents the degree of interaction between mobile ions and lattice and its variation with temperature sheds light on the suitable process for the

conduction mechanism. For an electrically heterogeneous structure with grain, grain boundary and sample–electrode interface, low-frequency conductivity is due to sample-

electrode interface, mid frequency due to grain boundary and high frequency as the bulk effect is a typical of thermally assisted tunneling between localized states.[34] σ in the high-

frequency region is described by UDR (Universal Dielectric Response) given by the equation, $A(i\omega\tau)^\beta$.[35] The variation of β with temperature can be taken as a criterion for

conduction mechanism.[36] According to Jonscher's power law if β decreases with T it indicates hopping conduction mechanism.[37] If β increases with the temperature a small

polaron is the predominant mechanism, whereas the large overlap polaron is characterized by a minimum followed by an increase of β with a further increase of the temperature. In cases

when β is temperature independent a quantum mechanical tunneling is expected. According to Funke when β is equal to 1 then the hopping motion involves a translational motion with

sudden hopping and when $\beta > 1$ then the motion involves localized hopping in the neighborhood without leaving its position.[37] The frequency at which change in slope takes

place is known as the hopping frequency of polarons, ω_p which is temperature-dependent. Thus ac conductivity follows Almond West relation, $\sigma(\omega) = A\omega_p[1+(\frac{\omega}{\omega_p})^\beta]$ ----- (7) where ω_p is the hopping frequency and β is the Jonscher's constant.[38] [39] As $A\omega_p = \sigma_{dc}$ according to (7) takes the form $\sigma(\omega) = \sigma_{dc} [1+ (\frac{\omega}{\omega_p})^\beta]$. [37] The high-frequency variation of σ_{ac} was found to obey Jonscher's power law, $\sigma_{ac} = A(\omega)^\beta$,----- (8), where ω is the angular frequency of the ac field.[40] The plot of $\ln \sigma_{total}$ vs. $\ln \omega$ (Fig. 6a) shows frequency-independent ac conductivity at very low frequency ascribed as dc conduction (σ_{dc}) and dispersion of ac conductivity at higher frequencies is seen with the change of slope at a frequency known as hopping frequency (ω_p) which is shifted to higher frequency side with an increase of temperature for all samples.

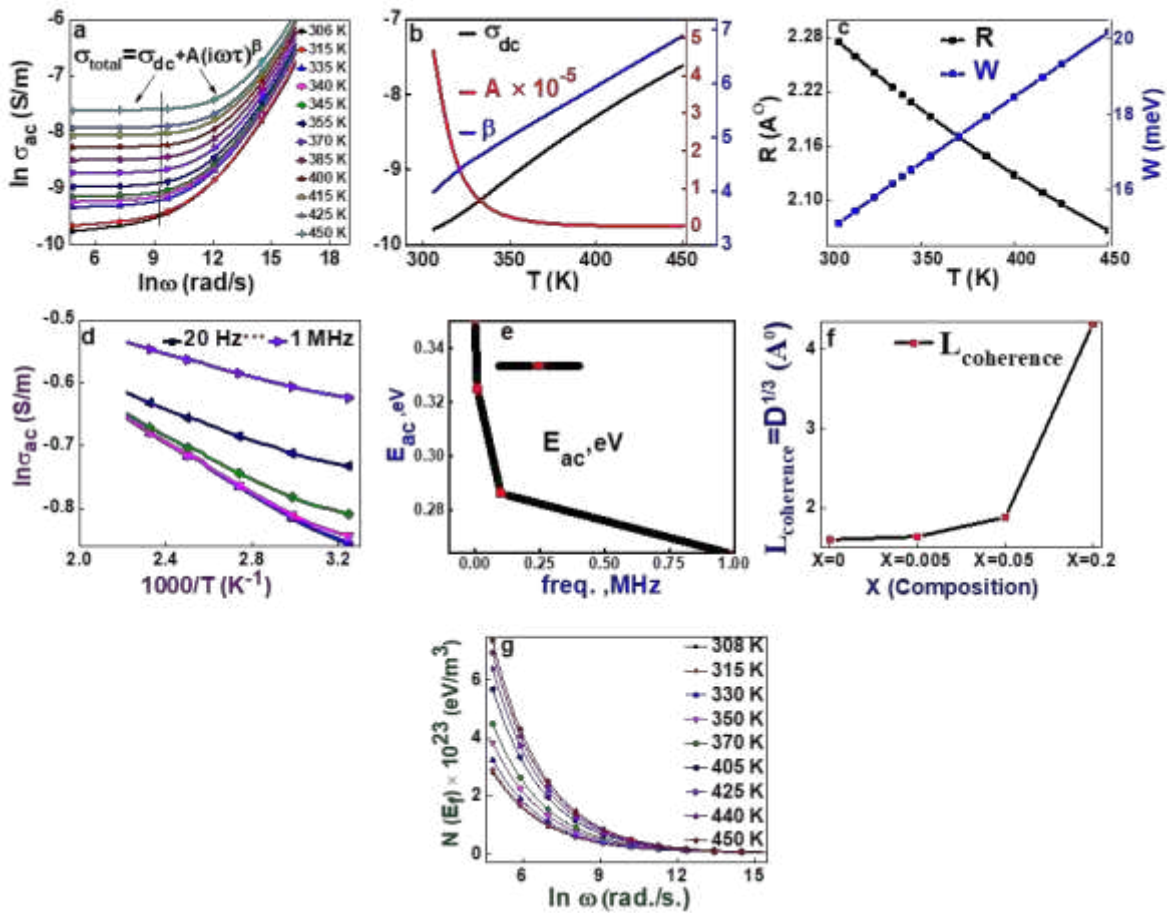


Fig. 6. Variation of (a) $\ln \sigma_{total}$ vs. $\ln \omega$ at few T's, (b) σ_{dc} , A and β vs. T, (c) Hopping range, R and Hopping energy, W vs. T, (d) $\ln \sigma_{ac}$ vs. $1000/T$, (e), E_{ac} vs. frequency, (f) L_{coh} vs. Composition and (g) $N(E_f)$ vs. $\ln \omega$ for CaCu₃Ti₄O₁₂.

By nonlinear fitting $\ln \sigma_{\text{total}}$ vs. $\ln \omega$ at various temperatures σ_{dc} , A , the strength of polarizability and β can be determined. The plot of σ_{dc} , β , and A vs. T in the Fig. 6b shows an increase of σ_{dc} and β with temperature. The increase of β with T clues small polaronic conduction as the dominant conduction mechanism. Here β is greater than 1 (here $\beta \approx 5.44$) indicates localized hopping motion of small polarons without changing neighborhood position.[37]

Also, coherence length, L (radius of polaron), called the size of polarization cloud, $L_{\text{coherence}} = D^{1/3}$ was calculated which was less than the lattice parameter for all compositions again indicating small polaron hopping conduction.[41] Thus strongly favors the result got from power law as shown in Fig. 6f for various compositions. The Plot of σ_{ac} vs. $1000/T$ obeys Arrhenius law (Fig. 6d). Its linear fit shows $E_{\text{a}\sigma_{\text{ac}}}$ which were found to decrease with increasing frequency as shown in inset Fig. 6e. This signifies an increase in ac conductivity with frequency, contributes minute loss in high-frequency zone.[34] Thus justifying Figs. 4b, 4d, 5b, 5d, S2b, S2d, S3b, S3d. Fig. 6a shows, the rapid increase of the high frequency ac conductivity for higher temperatures as compared to low T 's. This strongly favors that ac conductivity is due to polaronic conduction which is both temperature and frequency-dependent. Due to lagging of polaronic conduction loss occurs with increasing temperature and frequency which justifies the Figs. 4b, 4d, 5b, 5d, S2b, S2d, S3b, S3d. Polaronic relaxation means existence of UDR in high dielectric constant materials.[34]·[42] The plot of A vs. T in Fig. 6b shows a rapid decrease of strength of polarization ≈ 330 K then shows almost becomes temperature independent behaviour in high T zone. This explains the reason for the decrease in ϵ_r with temperature rise and further its temperature independency in high-temperature zone and rationalizes (Figs. 4a, 5a, S2a, S3a) very well. The ac conductivity data has been used to calculate the density of states, $N(E_f)$ at Fermi level using the relation $\sigma_{\text{ac}}(\omega) = \frac{\pi e^2}{3} \omega k_B T [N(E_f)]^2 \alpha^{-5} [\ln(\frac{f_0}{\omega})]^4$, --- (7), where e is the electronic charge, f_0 is the photon frequency, α is the localized wave function. Assuming $f_0 = 1013$ Hz and $\alpha = 1010$ m⁻¹ at various operating frequencies and temperatures.[37] The plot of $N(E_f)$ vs. $\ln \omega$ at various temperatures shows that the density of states increases with increasing temperature in the low-frequency zone and decreases exponentially in the high-frequency zone for all temperatures. So high $N(E_f)$ in low-frequency zone enables hopping between pairs of sites thereby increase of loss in the low-frequency zone with temperature is seen. On similar note drastic decrease of density of states in the high-frequency zone decreases loss.

AC conductivity in the high-temperature zone can also be explained based on oxygen loss at high temperature, according to $O_o = \frac{1}{2}O_2 + V_o'' + 2e'$, where O_o , O_2 , V_o'' and e' represent oxygen at oxygen site in the lattice, oxygen gas, a doubly positively oxygen vacancy and negatively charged electron respectively following with Kroger-Vink notation of defects. The electron released in the process makes the material semiconducting.[14] In CCTO, Ti^3 and Ti^4 form Ti^3-O-Ti^3 bonds. Under the applied field, the 3d electrons in Ti^3 ions can hop to Ti^4 . The ionic radius (0.605 Å) of Ti^4 is smaller than (0.670 Å) of Ti^3 . The formation of Ti^3 will distort the lattice and will produce polaronic distortion. The relaxation time of polarons is larger than that of free electrons attributable to polaronic distortions. Meanwhile under the ac applied field, the polarons can transport from Ti^3-O-Ti^3 to the other Ti^3-O-Ti^3 as Ti^3-O-Ti^3 bond form a linked path, leading to ac conduction and loss.[34]

Thermally activated low-frequency dc conductivity DC conductivity can be explained on basis of Koop's model which states that low-frequency conductivity is due to enhanced charge carrier density (hopping of electrons, ions, clusters or polaronic type due to lattice defects, etc.) at sample-electrode interface and grain boundaries.[43] DC conductivity was calculated by nonlinear fitting of curve, $\sigma_{total} = \sigma_{dc} + A(i\omega\tau)^\beta$. σ_{dc} was found to be independent of frequency but increases with temperature as shown in Fig.6a. The dc conductivity behavior can be rationalized in

- 1.) Low-temperature zone: obeying Mott's variable range hopping and
- 2.) High-temperature zone: obeying Arrhenius nearest-neighbor hopping like behaviour, $\sigma_{dc} = \sigma_1 e^{(-E_a/k_B T)}$ in the low frequency, and high-temperature zone, where σ_1 is constant, E_a is the activation energy for hopping, k_B is the Boltzmann constant and T is the absolute temperature.[34]

Mott first pointed out that at a low temperature most frequent hopping process is not due to nearest neighbor and Mott's variable range hopping conduction sets in.[34] The VRH conduction mechanism is described by, $\sigma_{dc} = \sigma_0 e^{-(T_0/T)^{1/4}}$, --- 10, where σ_0 is the conductivity at infinite temperature and constant T_0 is given by $T_0 = \frac{24}{[\pi k_B N(E_f) \xi^3]}$, where $N(E_f)$ is the density of localized states at the Fermi level and ξ is the decay length of the localized wave function.[34]

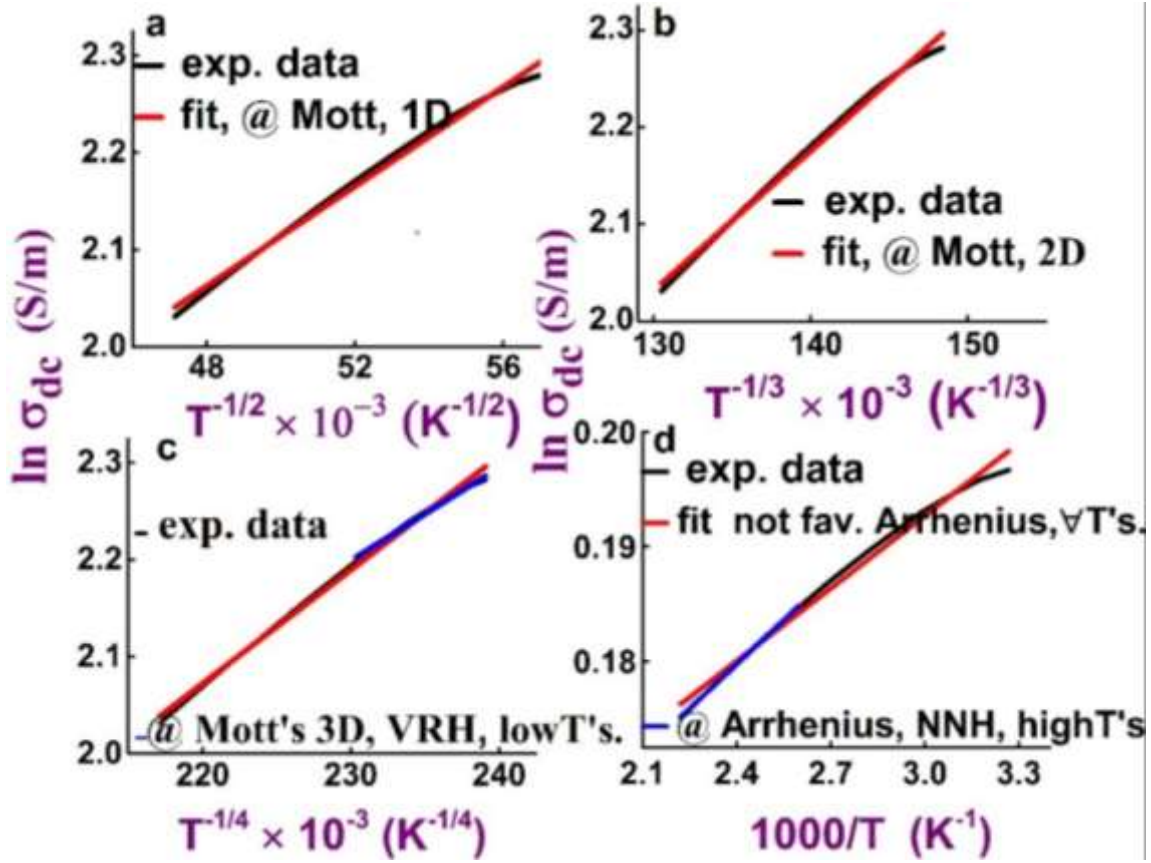


Fig. 7. σ_{dc} vs. (a) $T^{-1/2}$, (b) $T^{-1/3}$ (c) $T^{-1/4}$ (d) $1000/T$ for $\text{CaCu}_3\text{Ti}_4\text{O}_{12}$

Analyzing the results in terms of Mott's VRH model in which dc conductivity shows the temperature dependence of the type $T^{-1/S}$, where $S = \frac{1}{(d+1)}$ where d, dimensionality=1,2,3 for 1D, 2D and 3D hopping conduction case respectively. It was found that dc conductivity data deviates from a straight line fit for 1D and 2D case (Figs. 7a, 7b and 7d). However linear fit was obtained for $T^{-1/4}$ (Fig. 7c) only for low-temperature zone suggesting VRH hopping conduction via 3D polarons giving fitting parameters $\sigma_1 = 0.72589$ and $T_0^{1/4} = 11.70592 \text{ K}^{-(1/4)}$ or $T_0 = 1.9 \times 10^4 \text{ K}$. This temperature defines the energy scale $= k_B T_0 \approx (1.3 \times 10^{-23} \text{ J/K}) \times (1.9 \times 10^4 \text{ K}) \approx 3.38 \times 10^{-19} \text{ J} \approx 2.1 \text{ eV}$. So T_0 is the temperature which is closely related to the average energy needed to hop the localized charge carrier to nearest neighbor impurities at a certain distance R, the hopping range. As it is known that the ionization energy of hydrogen is 10 eV. So VRH is a low-temperature phenomenon (below room temperature) described by equation (10), where energy is insufficient to excite the charge carriers across the coulomb gap. In this temperature range conduction is by small polaron hopping in a small region in the vicinity of fermi energy. Mott's VRH mechanism

give two relations: - Hopping energy, $W = \frac{3}{[4\pi R^3 N(E_f) K_B T]}$, --- (11) and Hopping Range, $R = \frac{\xi^{1/4}}{[8\pi N(E_f) K_B T]^{1/4}}$, --- (12), where W is the Hopping energy, R is Hopping Range of polarons respectively. From equations (10), (11) and (12) One obtains, $W = 0.25 k_B T^{3/4} T_0^{1/4}$ --- (13). The density of states, $N(E_f) = 3.36 \times 10^{30} \text{ eV/m}^3$ was calculated using equation (9) by taking $\xi = a = 0.37 \text{ nm}$, the distance between neighboring Ti ions of CCTO.[34] It is clear now, dc conductivity was due to VRH of polarons in the very low-temperature zone, the hopping range of which decreases with temperature but hopping energy increases with temperature (Fig. 6c; W, R vs. T) and NNH of polarons (due to low, $E_{a\sigma dc} = 0.02 \text{ eV}$) in the high-temperature region both limited in low-frequency zone only are responsible for high loss in the low-frequency zone (Figs. 4d, 5d, S2d, S3d) So, power-law successfully explained the ac and dc conduction mechanism and its effect on dielectric behavior with temperature both in the low and high-frequency zone. Similar trends were followed by compositions, $x = 0.2, 0.05, 0.005$ shown in Figs. (S4-S6). Computed parameters $T_0 \text{ K}, E = k_B T_0 \text{ eV}$ (due to Mott), σ_{dc} vs. $T, E_{dc} \text{ (eV)}, (\beta, A)$ vs. $T, N(E_f)$ for $\text{CaCu}_3\text{Ti}_4\text{O}_{12-x}\text{I}_x$ ($x = 0, 0.005, 0.05$ and 0.2) are tabulated in Table S3.

3.5. Impedance Analysis A ceramic piece consists of small crystallites called grains joined randomly with strained and mismatch bonds. Properties of grain boundary differ from grains. For device applications, the electrode is required. Thus, an electronic component may now be treated as a grain-grain boundary-electrode system. Properties of these are distinct and highly sensitive to processing variables as heating-cooling rates, atmosphere, starting ingredients, etc. Interplaying with these desired properties can be achieved. High permittivity in BLCs unlike ferroelectrics or relaxors (which shows high permittivity due to polarization) may be associated with sample geometry, thin layer effects associated with grain, grain-boundary and sample-electrode interface governed by the equation $C = \frac{\epsilon_0 \epsilon' A}{d}$, (14) where ϵ' is the overall permittivity of dielectric regions, A , the cross-sectional area and d its thickness. Equation (14) is inherently used for the construction of high permittivity devices as BLC's with electrically heterogeneous microstructure. The compositional variations responsible for characteristics properties of ceramics present at grain surfaces are rather impossible to determine from electron microscopy. The experimental tool to probe the origin of high permittivity in CCTO via distinguishing the bulk, grain boundary contributions characterization was needed. All these can be excellently featured in electrical microstructure through impedance analysis, it measures the response of materials to the applied sinusoidal

voltage. Table S1 shows the wide range of phenomenon which can be studied ranging from low-frequency electrochemical processes to high-frequency effects associated with dielectric relaxations and ion hopping between.[44]

The various phenomena are characterized by the difficulty and/or the frequency of their occurrence. Thus, lattice vibrations occur at the infrared frequency (10^{12}) without elapsing time. Whereas long-range ionic conduction occurs by hopping of ions at lattice vibration frequencies dwelling a substantial amount of time before carrying out another hop. This overall hopping process (ionic or electronic) may be measured as sample resistance (R), a high resistance simply indicates occasional hops! Also, the thin layer (interfaces) associated with sample-electrode, grain boundary, and conducting grains have a capacitive effect which effectively measures the lattice polarization. Such processes involving a combination of lattice polarization and ionic/electronic transport through different regions of the sample may be represented as a combination of parallel RC elements.[44] The various phenomena in the frequency spectrum are identified by their magnitude of RC products or relaxation time, τ through $\omega\tau=1$. In IS most instrumentation covers several decades of frequency, ω , typically 10^{-2} to 10^6 Hz, allowing relaxation times, τ between 10^2 to 10^{-6} s⁻¹ to be studied. Since many phenomena tabulated are temperature-dependent, so to do a good judgement, different regions of the conductivity spectrum should be accessed by varying temperatures. Precisely low frequency (large τ) effects may be retrieved at higher temperatures at which the reactions are speeded up adequately for their relaxation frequencies to be within the measuring range: equally say local hops which occur very easily can be accessed by reducing temperature increasing the dwelling time between hops thereby the resistance associated with such processes.[44] So, characterizing via impedance spectroscopy provides powerful insight into the electrical microstructure. This way ferroelectric and non-ferroelectric components can be distinguished.

To understand the dielectric behavior of the material it is necessary to separate the various resistive and capacitive parts. Impedance spectroscopy is being widely used to extract contributions of these to the overall property of a ceramic. The dielectric behavior of a system can be revealed by four immittance functions: Impedance: $Z^*=Z'-iZ''$, admittance $^*=Y'+Y''=(Z^*)^{-1}$ and modulus $^*=(\epsilon^*)^{-1}=(i\omega C_0 Z^*)=M'+iM''$, complex dielectric constant $\epsilon^*=(I \omega C_0 Z^*)^{-1}=\epsilon'+\epsilon''$ where C_0 is the capacitance of empty cell used to house the sample, $\omega=2\pi f$ is the angular frequency, $i=\sqrt{-1}$ and Z' , M' and Z'' , M'' represent the real and imaginary part of respective functions. Immittance analysis is carried out in two modes (i)

complex plane (Z'' vs. Z') or modulus analysis (M'' vs. M') over a wide range of frequency and one gets one, two or three semicircular arc depending upon the contribution of grains, grain boundaries, sample electrode interface. The charge transfer process can be inferred by looking at the shapes of these arcs. In Z'' vs. Z' , the intercept of arcs with real axis gives the resistance of grain (high frequency), grain boundary (intermediate frequency), and sample electrode interface (low frequency). In M'' vs. M' plot, the intercept on the real axis varies inversely with the capacitive contribution of that part. The value of the resistance can be deduced using $\omega^*RC=1$, where ω^* is the angular frequency at the peak of the arc and C is the capacitance of that contribution.[14] The relaxation time, τ for one charge transfer process/polarization process is given by $\tau = RC = \frac{1}{\omega^*}$. If the relaxation process has a single value of relaxation time then one gets one semicircular arc with center on the real axis, for the number of relaxation times depressed semicircular arcs corresponding to that process is observed. The angle that the line joining the center of the circle to the origin makes with the real axis is the measure of the distribution of relaxation time.[14] A charge transfer process would have a certain time constant and would respond in the corresponding frequency region. A parallel RC circuit has one time constant signifying one charge transfer process. The impedance of this model circuit is given as; $Z' = \frac{R}{1+(\omega CR)^2}$, $Z'' = \frac{\omega CR^2}{1+(\omega RC)^2}$ ----- (15)

Z'' vs. Z' satisfying the relation;

$$\left(Z' - \frac{R}{2}\right)^2 + Z''^2 = \frac{R^2}{4} \text{ ----- (16)}$$

which is an equation of a circle having a center at point $(\frac{R}{2}, 0)$, radius equal to $\frac{R}{2}$, intercept with Z' axis at point $(R, 0)$ and passing through the origin in Z'' vs. Z' axis. As the values of R and C are positive, the Z'' vs. Z' plot will be a semicircle, with a peak point occurring at $Z' = \frac{R}{2}$. At this point, $Z'' = \frac{R}{2}$. Thus, if the values Z' and Z'' for a sample are experimentally measured in the certain frequency range and the complex plane plot is found to be a clear semicircular arc, then the parallel RC circuit model may be used to characterize the electrical behavior of the sample. The value of the intercept of the extrapolated arc with the Z' axis towards the low-frequency side will give the value of R . The value of C can be obtained using equation $\omega^*RC=1$, where ω^* is the frequency of peak position of arc. For this model, M'' and M' are given as

$$M' = \omega C_0 \left(\frac{\omega CR^2}{1+\omega^2 C^2 R^2} \right), \quad M'' = \omega C_0 \left(\frac{R}{1+\omega^2 C^2 R^2} \right) \text{----- (17)} \quad \text{which satisfy the relation}$$

$$\left(M' - \frac{C_0}{2C}\right)^2 + M''^2 = \left(\frac{C_0}{2C}\right)^2 \text{----- (18)}$$

This indicates that M'' vs. M' plot will be a semicircular arc passing through the origin and having an intercept at $M' = \frac{C_0}{2C}$ and center at $(\frac{C_0}{2C}, 0)$. On this plot, M'' would peak at the frequency where $\omega^*RC = 1$. Value of $M' = \frac{C_0}{2C}$ at $\omega = \infty$. Thus by using M'' vs. M' plot of the same experimental data can be obtained by noting the high-frequency intercept in the M'' vs. M' plot. The value of R can be obtained by using this value of C and noting the frequency where M'' peaks.[45]

Second mode of analysis (ii) Impedance or Modulus Spectroscopy process. In immittance analysis, Z'' and M'' vs. $\log f$ is plotted. If the relaxation time ($\tau = RC$) for the different process are widely different, then one observes a peak corresponding to each process. The peak position gives the relaxation frequency. Height of the peak in Z'' vs. $\log f$ gives $\frac{R}{2}$ at which loss is maximum. Z'' vs. $\log f$ highlights the process with maximum resistance (grain boundary or electrode specimen interface). Height of the peak in M'' vs. $\log f$ is given by $\frac{C_0}{2C}$, where C_0 is the capacitance of empty cell with air as dielectric and C is the capacitance with dielectric. Since these immittance functions have inverse relations, they can be used simultaneously to focus on certain information that is being suppressed in other representations. Complex plane plots are convenient to extract the capacitance and dc resistance of various contributions thereby dc conductivity can be measured. Whereas spectroscopic plots give the relaxation frequencies. Impedance and modulus plots give complementary information. Impedance plots highlight the process with maximum resistance (grain boundary or electrode specimen interface), while the modulus plot highlights the process with the least capacitance (grain or bulk contribution). If the capacitance is in the range \approx pf then the contribution is due to bulk (grain) bulk and if \approx nf then capacitance is due to grain boundary. $C_{gb} > C_g$ indicates well-sintered ceramics with narrow grain boundary.[46]

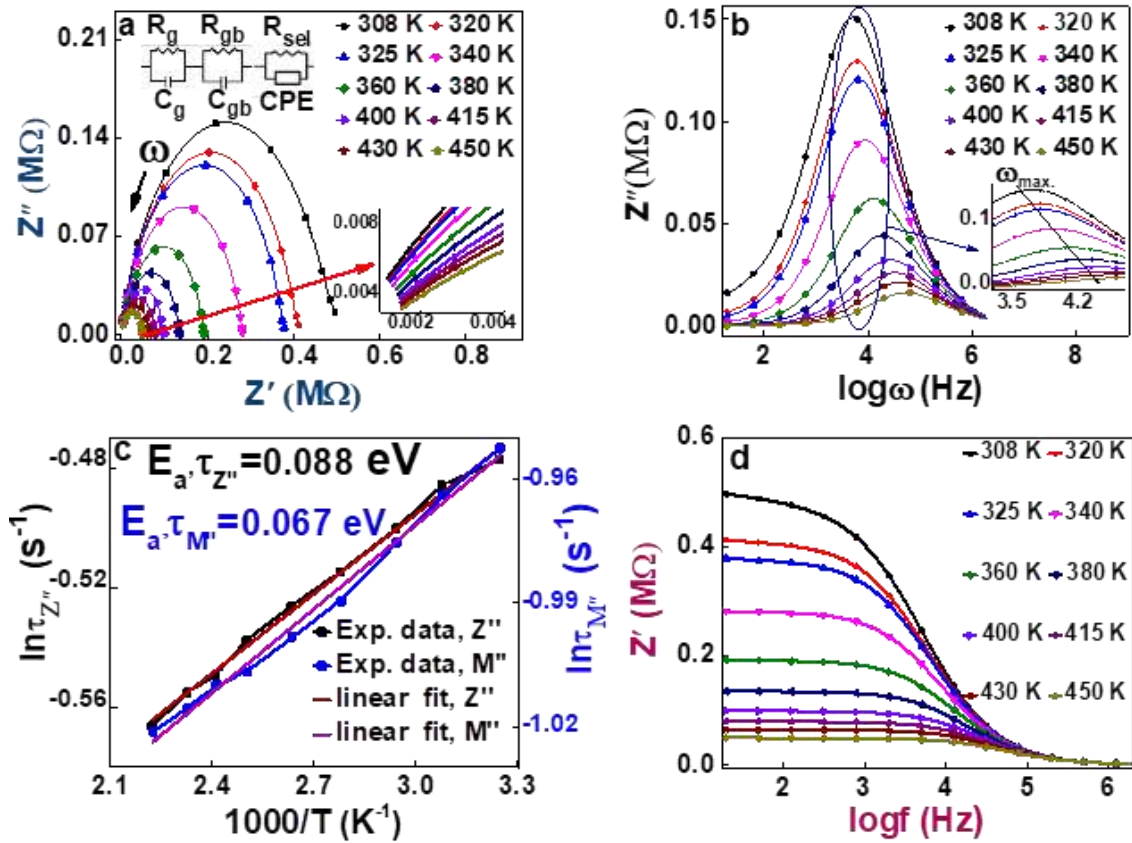


Fig. 8. (a) Z'' vs. Z' , (b) Z'' vs. $\log f$ at few steady temperatures, (c) $\ln \tau_{Z'', M''}$ vs. $1000/T$ and (d) Z' vs. $\log f$ for $\text{CaCu}_3\text{Ti}_4\text{O}_{12}$.

Fig. 8a (Z'' vs. Z') at all temperatures shows non-zero intercept (inset 8a) at high frequencies infers electrical heterogeneity of the ceramic in the low-frequency regime, low-temperature arcs with large slope indicate high $R_{s-el,gb,g}$, and thereby low loss. Using EIS software a model comprising (two RC's and one R-CPE) circuit representing grain-grain boundary-sample electrode system fitted the data well in Z'' vs. Z' at various temperatures and values of R_g , C_g (bulk contribution) R_{gb} , C_{gb} , (grain boundary) C_{sel} R_{sel} (sample electrode interface) were deduced. The presence of a linear portion in the immittance plot too flagged the presence of series CPE (Constant Phase Element) in the model. Depressed looking immittance plots indicates that parallel CPE to be included in the model.[46] CPE represents the distribution in the properties. CPE is a mathematical realization of the system in which the phase angle between the applied ac voltage and the resulting current remains independent of frequency[47]·[48] There are other views for possible sources of CPE, like CPE indicates inhomogeneity in electrode or formation of electrical double layer capacitor, but majority favors that CPE behavior arises due to the presence of distribution in time constants in the sample-electrode.[46]·[45] This makes ubiquitous use of CPE in impedance spectroscopy.

Analysis of grain and grain boundary behavior in $\text{CaCu}_3\text{Ti}_4\text{O}_{12}$ synthesized via solid-state route and sintered at 1050 °C for 12 hours

In general, for $\frac{R_{gb}}{R_g}=1$ and for widely separated time constants, i.e., $\frac{\tau_{gb}}{\tau_g}=100$ two clear arcs appear indicating the presence of two processes. ii) For $\frac{\tau_{gb}}{\tau_g}>1 \leq 5$, depressed-looking arc appears and $\frac{\tau_{gb}}{\tau_g}=1$, i.e. time constants for different relaxation processes are not widely separated only one semicircular arc appears for all temperatures.[45] For CCTO sintered at 1050 °C, 12 hours $\frac{R_{gb}}{R_g}$ was calculated to be 1-6 and $\frac{\tau_{gb}}{\tau_g}=1$ at various temperatures indicates that relaxation time for three processes are not widely different and therefore only one arc for the normalized impedance plane plot $\frac{Z''}{(R_g+R_{gb})}$ vs. $\frac{Z'}{(R_g+R_{gb})}$ and normalized modulus plane plot $\frac{M''}{\{(Co/R_g+R_{gb})\}}$ vs. $\frac{M'}{\{(Co/(R_g+R_{gb}))\}}$ appeared as shown in Figs. 9a and 9b for CCTO. In practice, Z'' vs. Z' plots contain well resolved semicircular type depressed arcs when the time constant are widely different whereas a hump appears when the time constant is not widely different.[48] In Fig. 8a, Z'' vs. Z' plots shows hump at all T's strongly favoring that relaxation time for various relaxation processes are not widely different.

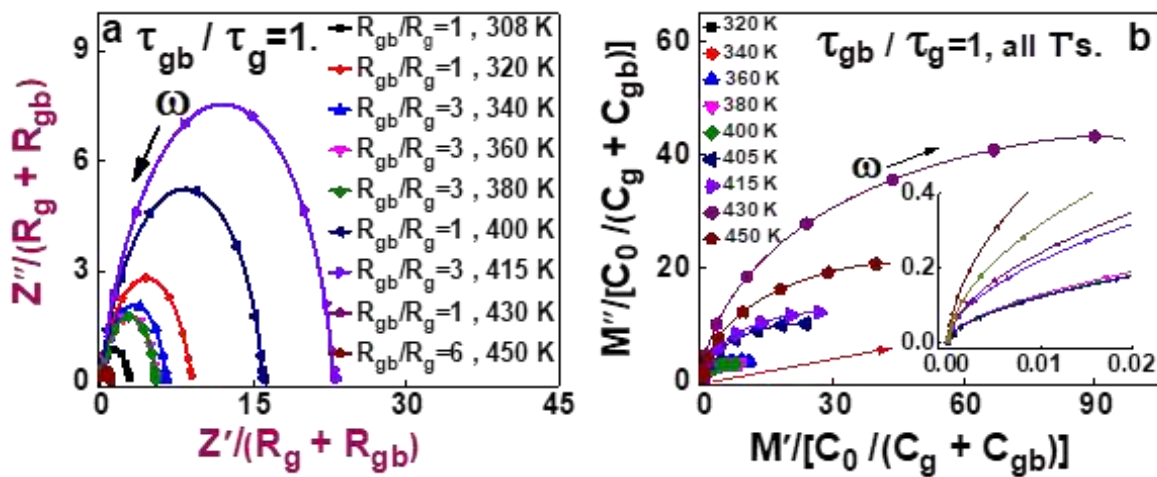


Fig. 9. Normalized plots for $\text{CaCu}_3\text{Ti}_4\text{O}_{12}$ (a) $\frac{Z''}{(R_g+R_{gb})}$ vs. $\frac{Z'}{(R_g+R_{gb})}$ and (b) $\frac{M''}{\{(Co/R_g+R_{gb})\}}$ vs. $\frac{M'}{\{(Co/(R_g+R_{gb}))\}}$

Over in (Fig. 8a), the decreasing diameter of the semicircular arcs of non-zero intercept with increasing temperature indicates a decrease in R_g , R_{gb} , R_{s-el} (high, mid, and low-frequency response), which reduces the barrier to the motion of charge carriers increasing electrical

transport and increasing ac conductivity thereby contributing loss with frequency rise in their respective frequency zone, also verified by $\ln \sigma_{ac}$ vs. $\ln \omega$ plot, (Figs. S4a – S6a) from where it was found that activation energy for ac conductivity decreases with the increase of frequency enhancing conductivity which is the cause of loss in the high-frequency regime. In the plot Z'' vs. Z' , Fig. 8a, the center of the fitted semicircle lies below the abscissa indicating a departure from pure Debye type and confirming the Jonscher's universal power law. The inclination of a semicircle with respect to real axis with increasing temperature indicates that departure from Debye nature was partly thermally assisted.[49][50] In Figs. 8b and S7b, Z'' vs. $\log f$, shows broad and asymmetrical peak around (Z''_{max}) which gets broader and shifts to high-frequency side with temperature rise, the peak broadening suggests spread of relaxation times i.e. existence of various temperature-dependent electrical relaxation phenomenon in the material. Also, peak shifting points that it is a thermally activated process (non-Debye type). Again the merging of Z'' values at high frequency may be due to accumulation of charge carriers at interfaces (space charge) in the material. The most probable relaxation time $\tau_m = \frac{1}{\omega_m}$ obeys Arrhenius law, $\omega_m = \omega_0 e^{-E_a/k_B T}$, where ω_0 is the pre-exponential factor, k_B is the Boltzmann constant, give the activation energy ($E_{a\omega Z''} \approx 0.087$ eV) for most probable jump frequency. It's attention-grabbing that $E_{a\omega Z''}$ (Fig. 8c) represents dielectric relaxation (for localized conduction).[25] The relaxation process may be due to immobile charges/electrons at low temperatures and defects at high temperatures.[47] At high-temperature zone the relaxation time, τ is less (means faster electrical relaxation process via defects). In Fig. 8d, Z' vs. $\log f$, Z' (resistance) of the sample decreases with a sudden dip (due to sudden decrease in DOS, $N(E_f)$) with an increase of temperature in low-frequency zone exhibiting (NTCR) type behavior analogous to semiconductors and merge with very low magnitude plateau in higher frequency zone, for all temperatures which are due to release of space charge by decreasing potential barrier with increasing temperature. Thus enhancing ac conductivity with an increase of temperature at high frequencies, which again very well explains loss behavior in the high-frequency zone.[51] A similar explanation holds for $\text{CaCu}_3\text{Ti}_4\text{O}_{0.995}\text{I}_{0.005}$.

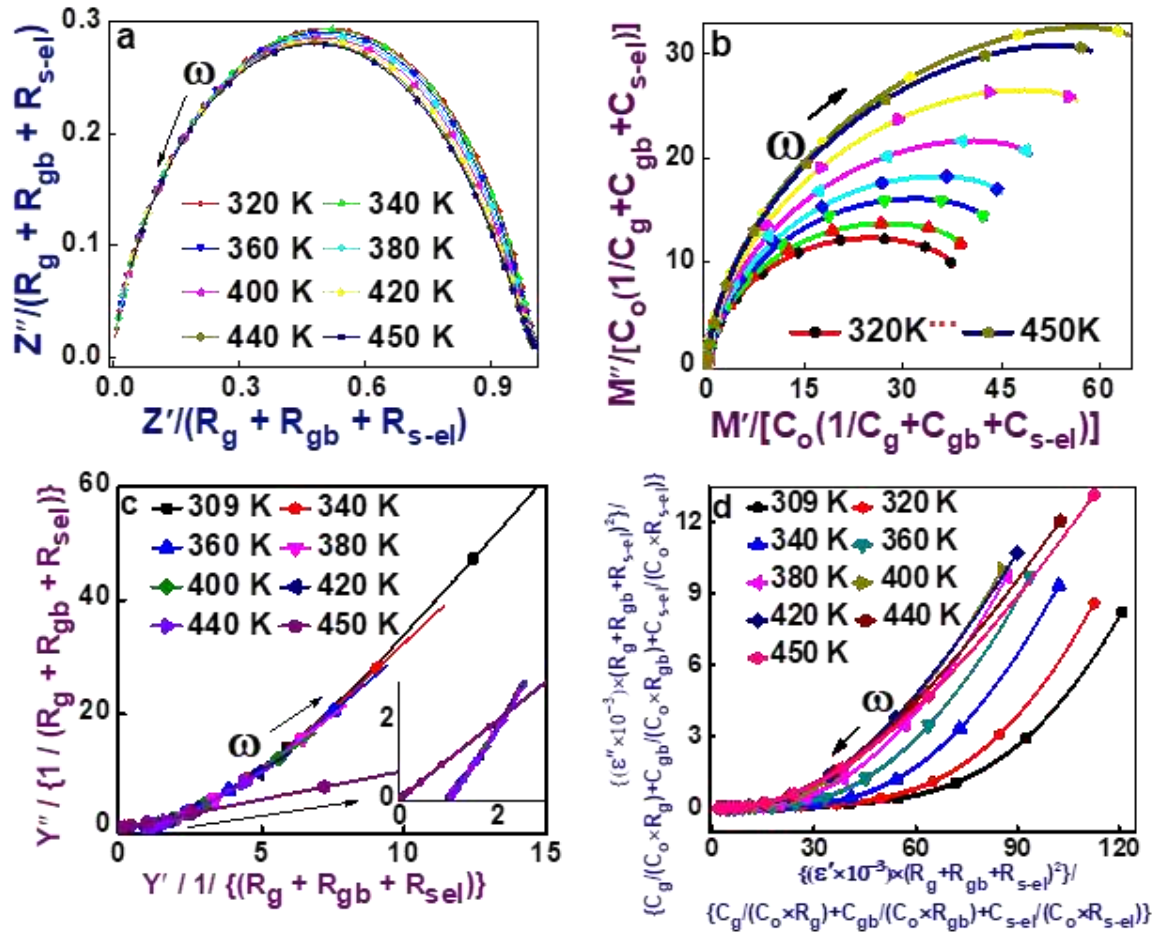


Fig. 10. Normalised,

$$(a) \frac{Z''}{(R_g + R_{gb} + R_{s-el})} \text{ VS. } \frac{Z'}{(R_g + R_{gb} + R_{s-el})}, \quad (b) \frac{M''}{C_o \{1/(C_g + C_{gb} + C_{s-el})\}} \text{ VS. } \frac{M'}{C_o \{1/(C_g + C_{gb} + C_{s-el})\}}$$

$$(c) \frac{Y''}{(R_g + R_{gb} + R_{sel})} \text{ VS. } \frac{Y'}{(R_g + R_{gb} + R_{sel})},$$

$$(d) \frac{\epsilon''}{\{[C_g/C_o \times R_g / (R_g + R_{gb} + R_{sel})]^2 + [C_{gb}/C_o \times R_{gb} / (R_g + R_{gb} + R_{sel})]^2 + [C_{sel}/C_o \times R_{sel} / (R_g + R_{gb} + R_{sel})]^2\}} \text{ VS. } \frac{\epsilon'}{\{[C_g/C_o \times R_g / (R_g + R_{gb} + R_{sel})]^2 + [C_{gb}/C_o \times R_{gb} / (R_g + R_{gb} + R_{sel})]^2 + [C_{sel}/C_o \times R_{sel} / (R_g + R_{gb} + R_{sel})]^2\}} \text{ for } \frac{R_{gb}}{R_g}$$

$$= 1-4, \quad \frac{\tau_{gb}}{\tau_g} = 4-6 \text{ and } \frac{R_{gb}}{R_{s-el}} = 5-6 \text{ and } \frac{\tau_{gb}}{\tau_g} = 28-30 \text{ for } \text{CaCu}_3\text{Ti}_4\text{O}_{0.995}\text{I}_{0.005}.$$

Analysis of grain and grain boundary behavior in $\text{CaCu}_3\text{Ti}_4\text{O}_{0.995}\text{I}_{0.005}$.

In $\text{CaCu}_3\text{Ti}_4\text{O}_{0.995}\text{I}_{0.005}$ at low temperatures, $\frac{R_{gb}}{R_g} = 1-4$ and time constants, $\frac{\tau_{gb}}{\tau_g} = 4-6$ and few high temperatures, $\frac{R_{gb}}{R_g} = 5-6$ and $\frac{\tau_{gb}}{\tau_{s-el}} = 28-30$, signifying not much difference among the grain boundary, grain and sample-electrode resistance and their corresponding time constants at various T's. The normalized plot of Z'' vs. Z' (Fig. 10a) for $\text{CaCu}_3\text{Ti}_4\text{O}_{0.995}\text{I}_{0.005}$ gave a

single humpy semicircular arc signifying the presence of one charge transfer/polarization process. Whereas the corresponding M'' vs. M' Fig. 10b plot shows a flattening trend towards the high-frequency side indicating more polarization processes. This indicates that inference derived from one formalism might lead to erroneous results. So plots with other formalisms should be looked along with. The Y'' vs. Y' plots (Fig. 10 c) and ϵ'' vs. ϵ' (Fig. 10d) result in nearly straight line indicative of more polarization processes with a narrow distribution of time constants.[46][45] The behavior of CCTO and $\text{CaCu}_3\text{Ti}_4\text{O}_{0.995}\text{I}_{0.005}$ are in a quite close resemblance.

Scaling Behavior The Nyquist plot (Z'' vs. Z') is useful for materials which possess one or more widely separated relaxation process of comparable magnitudes and obey Debye law.

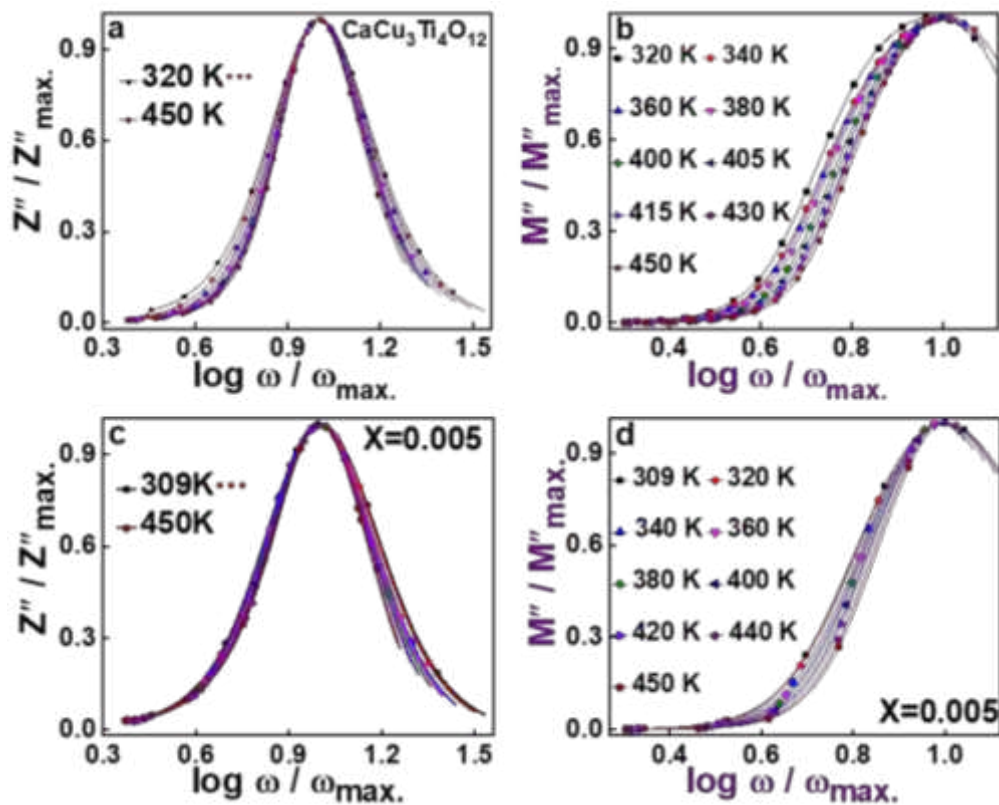


Fig. 11. Scaling behavior of Z'' and M'' vs. $\log \omega/\omega_m$ for (a, b) CCTO and (c, d) $\text{CaCu}_3\text{Ti}_4\text{O}_{0.995}\text{I}_{0.005}$.

Figs.11a-d illustrate the plot of $Z''(\omega, T)$ and $M''(\omega, T)$ data in scaled coordinates i.e. $Z''(\omega, T)/Z''_{\max}$ vs. $\log \omega/\omega_m$ and $M''(\omega, T)/M''_{\max}$ vs. $\log \omega/\omega_m$ for CCTO at various temperatures, where ω_m corresponds to the peak value of Z'' and M'' vs. $\log f$ plot. The co-occurrence of all curves/peaks in scaled impedance and electric modulus master curve clearly indicates that the relaxation mechanism is nearly temperature independent. Also, the FWHM observed in both

plots is greater than 1.14 decades indicating relaxation to be temperature independent and non-exponential in nature.[49]

The shift of Z'' and M'' peaks with frequency in their spectroscopic plots Figs. 8b and S7b and Figs. 12b and S8b indicates relaxation to be non-Debye type (i.e. poly-dispersive). These behaviors can be described by Kohlraush-Williams-Watt function, $\varphi(t)$ which represents the distribution of relaxation time in ionic conductors.[52] The dielectric modulus can thus be represented by, $M^* = M_\infty [1 - \int dt. e^{-i\omega t} (d\varphi/dt)]$ ----- (19), where $\varphi(t) = e^{(-t/t_\infty)^\beta}$, where, $t_\infty = \frac{1}{2\pi f \beta}$ is called the conductivity relaxation time and β is the Kohlraush exponent which lies between 0 and 1, smaller the value of β , larger is the deviation from relaxation as compared to Debye-type relaxation. Such non-exponential type relaxation governed by the above equation suggests the possibility of hopping ion migration accompanied by time-dependent mobility of other charge carriers of the same type.[52]

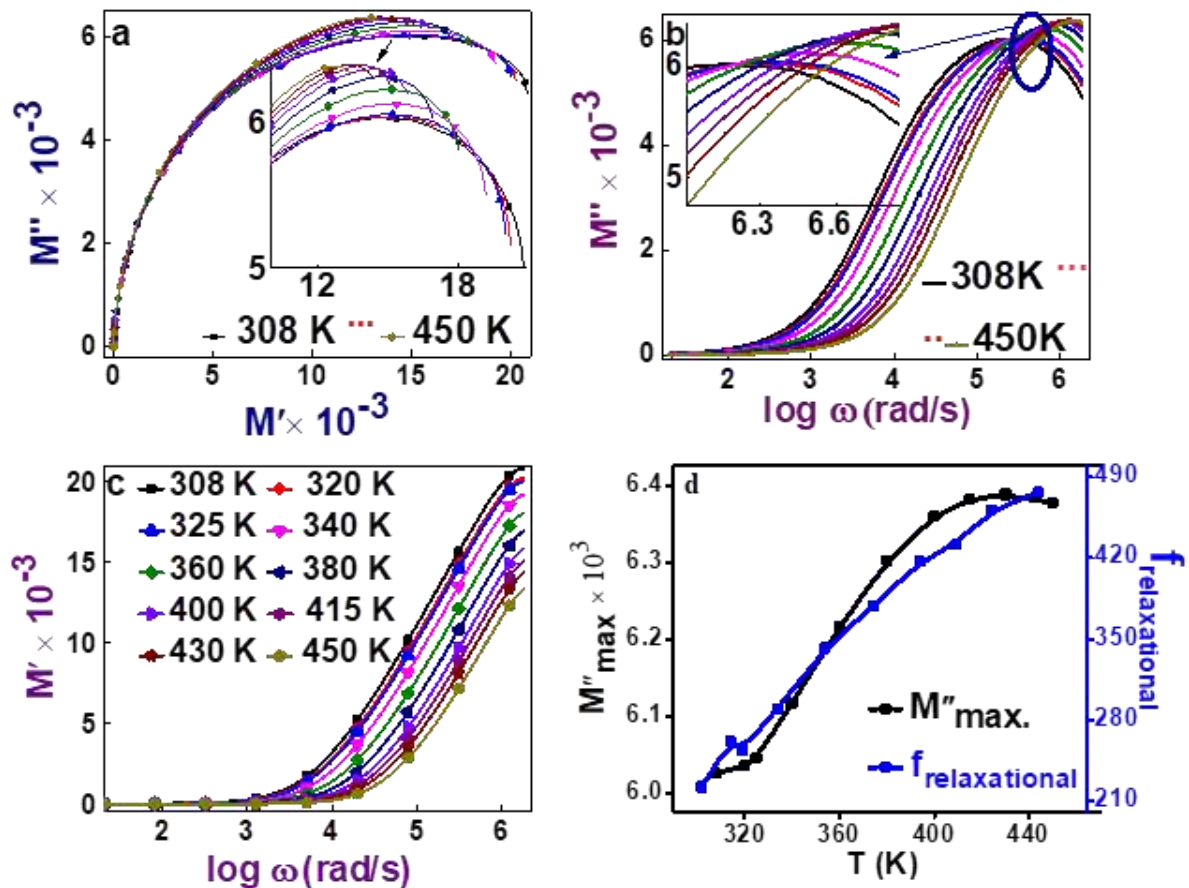


Fig. 12. Variation of (a) M'' vs. M' , (b) M'' vs. $\log \omega$, (c) M' vs. $\log f$ at few steady temperatures, (d) M'' and $f_{\text{relaxational}}$ vs. T for the composition $\text{CaCu}_3\text{Ti}_4\text{O}_{12}$

Modulus analysis for $\text{CaCu}_3\text{Ti}_4\text{O}_{12}$ In Fig. 12a, M'' vs. M' plot, one semicircle appears with the decreased diameter and high M'' value, with increase in temperature. This can be related to decrease in the contribution of grain-boundary resistance to the modulus total resistance with increase of temperature.[37]:[49] Information regarding electrical transport and polarization process can be collected via the electric modulus plot. In M' vs. $\log\omega$ (Fig. 12c), very low magnitude plateau in the low-frequency zone appears for all temperatures signifying negligible or absence of electrode polarization.[53]:[30] Further a sigmoidal increase in the value of M' , tending towards M_∞ , the asymptotic value in high-frequency zone showing dispersion signifies conduction due to short-range mobility of charge carriers (via ions).[49] If instead of dispersion, M_∞ had been saturated at higher temperatures in higher frequency zone then the conduction would have been through the long-range movement of charge carriers.[49]

$M''(\omega)$ exhibits a slightly asymmetric peak, ($M''_{\max.}$) at which relaxation occurs, shifts to a higher frequency with increasing temperature (Fig. 12b). The most probable relaxation time, τ_m follows Arrhenius law, gives activation energy, $E_{a\omega M''}=0.067$ eV. It's noteworthy that activation energy, $E_{a\omega Z''}$ represents localized conduction (i.e. dielectric relaxation) and that of $M''(E_{a\omega M''})$ represents nonlocalized conduction (i.e. long-range conductivity).[28] The twinning values of $E_{a\omega M''}=0.067$ eV and $E_{a\omega Z''}=0.081$ eV suggests that conduction and relaxation processes occur by the same type of charge carriers.[28] It is notable in $M''(\omega)$ (Fig. 12b) that, considering parameters, $M''_{\max.}$ the shift in f_{peak} suggests the variation in resistance, whereas the only variation in $M''_{\max.}$ with no change in f_{peak} suggests a change in both resistance and capacitance.[28] However, Fig. 12b shows variations in both parameters of $M''_{\max.}$ and f_{peak} indicating the variation in capacitance. The thin layer associated with grain and grain boundary and sample-electrode interface strongly support BLCs. Furthermore, both $Z''(\omega)$ (Figs. 8b and S7b) and $M''(\omega)$ (Figs. 12b and S8b) shows an overlapping in the high-frequency range (≈ 1 MHz) for all temperature range investigated, being characteristics of long-range conductivity process which is the reason for the loss in the high-frequency range[52] and similar explanation appears for $\text{CaCu}_3\text{Ti}_{0.995}\text{O}_{0.005}$, (Fig. S7).

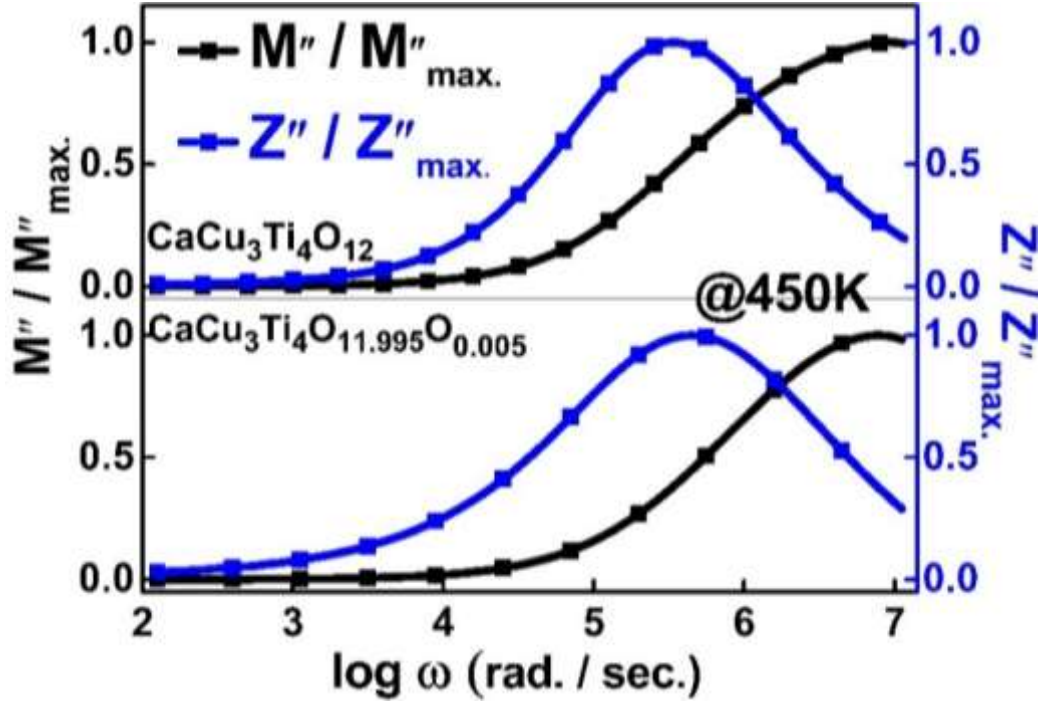


Fig. 13. Combined plot of $Z''/Z''_{\max.}$ and $M''/M''_{\max.}$ vs. $\log \omega$, for $\text{CaCu}_3\text{Ti}_4\text{O}_{12}$ and $\text{CaCu}_3\text{Ti}_{11.995}\text{O}_{0.005}$ at 450 K, respectively.

The combined plot of Z'' and M'' vs. $\log \omega$ for $\text{CaCu}_3\text{Ti}_4\text{O}_{12}$ and $\text{CaCu}_3\text{Ti}_{11.995}\text{O}_{0.005}$ shown in Fig. 13 provides information whether its localized/short range, (i.e .defect relaxation) or non-localized (i.e. ionic or electronic conductivity) that governs the relaxation process.[53] The mismatch in the peak frequency in M'' and Z'' indicates relaxation process is dominated by the short-range movement of charge carriers and deviates from ideal-Debye like behavior, while their overlap indicates the dominance of long range movement of charge carriers.[28] In Fig. 13 plot $Z''/Z''_{\max.}$ and $M''/M''_{\max.}$ vs. $\log \omega$, the mismatch in the peak frequencies for $\text{CaCu}_3\text{Ti}_4\text{O}_{12}$ and $\text{CaCu}_3\text{Ti}_{11.995}\text{O}_{0.005}$ suggests non-Debye like behavior and simultaneous occurrence of both long-range and localized relaxation with the short-range movement of charge carriers dominating. The long-range is dominated at a low frequency, which is known as dc conductivity in the absence of interfacial polarization. Localized electron is mobilized with the aid of lattice oscillation via hopping (Fig. 13). In addition the low magnitude of activation energy,(Figs.8c and S6c), $E_{a\omega Z''} = 0.088$ eV (for CCTO) and $E_{a\omega Z''} = 0.089$ eV (for $\text{CaCu}_3\text{Ti}_{11.995}\text{O}_{0.005}$), favors the charge transport via small polaron hopping mechanism in high-frequency zone.[53]

For one of the composition, $\text{CaCu}_3\text{Ti}_4\text{O}_{0.995}\text{I}_{0.005}$ it was found that R_g , R_{gb} , R_{s-el} decreases with temperature, (Fig. 14a).The time constants, $\tau_{s-el} > \tau_{gb} > \tau_g$, (Fig.14c and Table 2) obeys Arrhenius format and show NTCR behavior with the activation energies much larger as

compared to polarons. So clearly indicating it's the polarons hopping and lagging due to their low activation energies, managing the electrical behavior of $\text{CaCu}_3\text{Ti}_4\text{O}_{12-x}\text{I}_x$ dominantly.

Table 2. Tabulated values of $E_{a,\tau,Z''}$, $E_{a,\tau,M''}$, $E_{a,R_{s-el}}$, $E_{a,R_{gb}}$, E_{a,R_g} , $E_{a,\tau_{s-el}}$, $E_{a,\tau_{gb}}$, E_{a,τ_g} for $\text{CaCu}_3\text{Ti}_4\text{O}_{12}$ and $\text{CaCu}_3\text{Ti}_{11.995}\text{O}_{0.005}$

.Composition, x	$E_{a,\tau,Z''}$ (eV)	$E_{a,\tau,M''}$ (eV)	$E_{a,R_{s-el}}$ (eV)	$E_{a,R_{gb}}$ (eV)	E_{a,R_g} (eV)	$E_{a,\tau_{s-el}}$ (eV)	$E_{a,\tau_{gb}}$ (eV)	E_{a,τ_g} (eV)
$\text{CaCu}_3\text{Ti}_4\text{O}_{12}$	0.081	0.067	-	-	-	-	-	-
$\text{CaCu}_3\text{Ti}_{11.995}\text{O}_{0.005}$	0.089	0.07	0.95	0.97	0.52	1.2	1.19	0.9

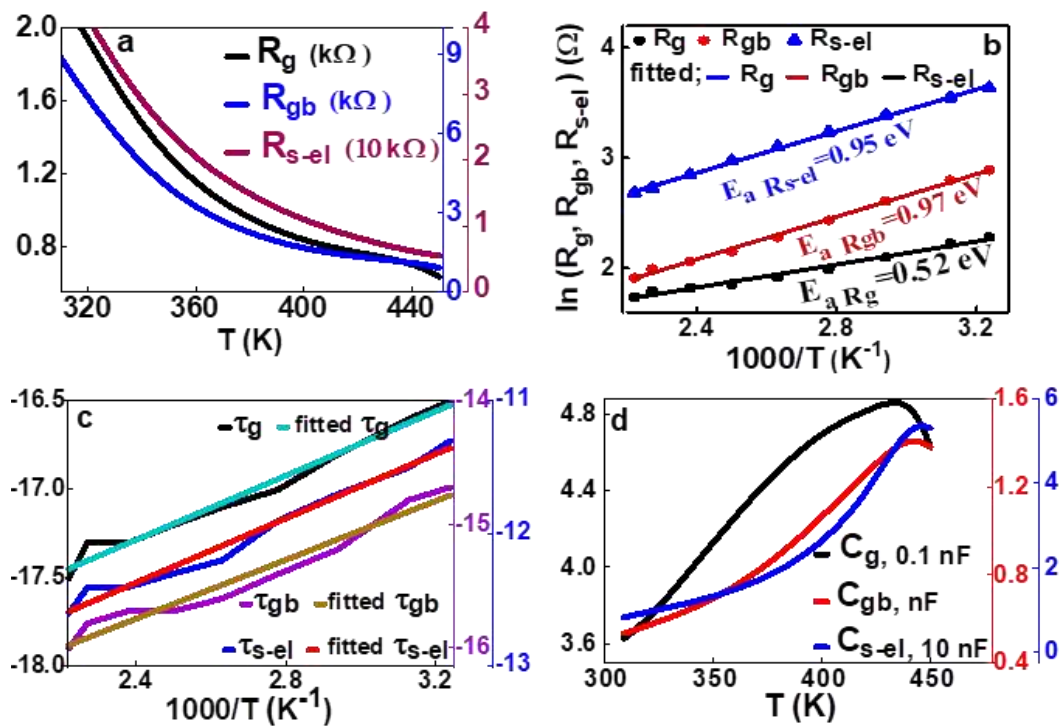


Fig. 14. Variation of (a) R_g , R_{gb} , R_{s-el} vs. T , (b) $E_{a,R_{gb}}$, $E_{a,R_{s-el}}$, E_{a,R_g} vs. $1000/T$, (c) $E_{a,\tau_{s-el}}$, $E_{a,\tau_{gb}}$, E_{a,τ_g} vs. $1000/T$, (d) C_g , C_{gb} , C_{s-el} vs. for $\text{CaCu}_3\text{Ti}_4\text{O}_{0.995}\text{I}_{0.005}$

4. Conclusions

Study of solid state synthesized $\text{CaCu}_3\text{Ti}_4\text{O}_{12-x}\text{I}_x$, ($x=0, 0.005, 0.05, 0.2$) reveals the origin of high permittivity value, factors effecting loss and their minimization. For one composition ($\text{CaCu}_3\text{Ti}_4\text{O}_{0.98}\text{I}_{0.2}$), the increase of dielectric constant by factor of 10 and decrease of loss by factor of 100 was achieved. CDC behaviour is due to large grain size of high C_g and formation of IBLC's. Maxwell-Wagner type relaxations with narrow distribution of time constants $\tau_{gb}/\tau_g=1=6$ were noticed, unlike Debye type. Thus supporting IBLC model due to

grain, grain boundary and sample electrode interface representing high, mid and low frequency zone, respectively. M' vs. $\log f$ and high value of $E_{a,\tau s-el} \approx 1.2$ clues negligible electrode polarization. High loss is due to dc conduction via small polarons hopping and loss can be minimized by maximizing R_{s-el} , R_{gb} and minimizing defects, oxygen vacancies at grain boundaries. Permittivity can be enhanced by increasing C_g thereby enhancing space charge polarization within grains. So further exhaustive study on grain engineering need to be done to make it a marketing competitor. Owing to a negligible loss at the high-frequency it demonstrates a potential application at high temperature and microwave frequencies.

Author contributions

BY: Methodology, Investigation, Conceptualization, Validation, Formal analysis, Writing original draft, preparation, Writing-review and editing. RK: Review & editing. KKK: Supervision, Writing-review and editing. MKG: Writing-review and editing.

Data availability

All data generated or analyzed during this study are included in this submission [and its supplementary information files].

Compliance with ethical standards

Conflict of interest The authors declare that they have no conflicts of interest.

References

- [1] D.C. Sinclair, T.B. Adams, F.D. Morrison, A.R. West, CaCu₃Ti₄O₁₂: One-step internal barrier layer capacitor, *Appl. Phys. Lett.* 80 (2002) 2153–2155.
<https://doi.org/10.1063/1.1463211>.
- [2] M.A. Subramanian, D. Li, N. Duan, B.A. Reisner, A.W. Sleight, High Dielectric Constant in ACu₃Ti₄O₁₂ and ACu₃Ti₃FeO₁₂ Phases, *J. Solid State Chem.* 151 (2000) 323–325. <https://doi.org/10.1006/jssc.2000.8703>.
- [3] A.. Ramirez, M.. Subramanian, M. Gardel, G. Blumberg, D. Li, T. Vogt, S.. Shapiro, Giant dielectric constant response in a copper-titanate, *Solid State Commun.* 115 (2000) 217–220. [https://doi.org/10.1016/S0038-1098\(00\)00182-4](https://doi.org/10.1016/S0038-1098(00)00182-4).
- [4] J. Wu, C.-W. Nan, Y. Lin, Y. Deng, Giant Dielectric Permittivity Observed in Li and Ti Doped NiO, *Phys. Rev. Lett.* 89 (2002) 217601.
<https://doi.org/10.1103/PhysRevLett.89.217601>.
- [5] D. Bharatiya, S. Kumar, S. Raghunandan, P. Paik, Dielectrics of graphene oxide decorated with nanocomposite silica-coated calcium copper titanate (CCTO) nanoparticles, *J. Mater. Sci.* 54 (2019) 6272–6285. <https://doi.org/10.1007/s10853->

019-03336-8.

- [6] D. Bharatiya, K. Santhosh Kumar, R. Seelaboyina, P. Paik, A detailed study on the dielectric properties of CCTO@SiO₂ core-shell nanoparticles: Role of SiO₂-NH₂ shell over CCTO core surface, *J. Solid State Chem.* 277 (2019) 346–355.
<https://doi.org/10.1016/j.jssc.2019.06.023>.
- [7] A.K. Rai, N.K. Singh, S.-K. Lee, K.D. Mandal, D. Kumar, O. Parkash, Dielectric properties of iron doped calcium copper titanate, CaCu_{2.9}Fe_{0.1}Ti₄O₁₂, *J. Alloys Compd.* 509 (2011) 8901–8906. <https://doi.org/10.1016/j.jallcom.2011.06.008>.
- [8] Z. Xu, H. Qiang, Z. Chen, Y. Chen, Dielectric behavior of Ba-doped CaCu₃Ti₄O₁₂ ceramics prepared from citrate–nitrate combustion derived powders, *J. Mater. Sci. Mater. Electron.* 26 (2015) 578–582. <https://doi.org/10.1007/s10854-014-2437-6>.
- [9] Z. Yang, L. Zhang, X. Chao, L. Xiong, J. Liu, High permittivity and low dielectric loss of the Ca_{1-x}Sr_xCu₃Ti₄O₁₂ ceramics, *J. Alloys Compd.* 509 (2011) 8716–8719. <https://doi.org/10.1016/j.jallcom.2011.06.039>.
- [10] J. Lee, J. Koh, Enhanced dielectric properties of Ag-doped CCTO ceramics for energy storage devices, *Ceram. Int.* 43 (2017) 9493–9497.
<https://doi.org/10.1016/j.ceramint.2017.04.130>.
- [11] M. Li, Q. Liu, C.X. Li, Study of the dielectric responses of Eu-doped CaCu₃Ti₄O₁₂, *J. Alloys Compd.* 699 (2017) 278–282.
<https://doi.org/10.1016/j.jallcom.2016.12.422>.
- [12] T. Li, J. Chen, D. Liu, Z. Zhang, Z. Chen, Z. Li, Effect of NiO-doping on the microstructure and the dielectric properties, *Ceram. Int.* 40 (2014) 9061–9067.
<https://doi.org/10.1016/j.ceramint.2014.01.119>.
- [13] J. Jumptam, B. Putasaeng, N. Chanlek, P. Kidkhunthod, P. Thongbai, S. Maensiri, P.

- Chindaprasirt, Improved giant dielectric properties of $\text{CaCu}_3\text{Ti}_4\text{O}_{12}$ via simultaneously tuning the electrical properties of grains and grain boundaries by F – substitution, *RSC Adv.* 7 (2017) 4092–4101. <https://doi.org/10.1039/C6RA27381E>.
- [14] O. Parkash, B. Yadav, P. Singh, D. Kumar, Barrier Layers Formation in Tin Substituted Calcium Copper Titanate $\text{CaCu}_3\text{Ti}_{4-x}\text{Sn}_x\text{O}_{12}$ ($0 \leq x \leq 1.0$), *J. Phys. Soc. Japan.* 75 (2006) 094717. <https://doi.org/10.1143/JPSJ.75.094717>.
- [15] A. Kumar, N. Kumar, S. Kumar, L. Singh, K.D. Mandal, Effect of tantalum substitutions on microstructures and dielectric properties of calcium copper titanate ($\text{CaCu}_3\text{Ti}_4\text{O}_{12}$) ceramic, *Mater. Sci. Eng. B.* 177 (2012) 1213–1218. <https://doi.org/10.1016/j.mseb.2012.06.002>.
- [16] R. Xue, Z. Chen, H. Dai, D. Liu, T. Li, G. Zhao, Effects of rare earth ionic doping on microstructures and electrical properties of $\text{CaCu}_3\text{Ti}_4\text{O}_{12}$ ceramics, *Mater. Res. Bull.* 66 (2015) 254–261. <https://doi.org/10.1016/j.materresbull.2015.02.058>.
- [17] S. Rani, N. Ahlawat, R. Punia, K.M. Sangwan, P. Khandelwal, Dielectric and impedance studies of La and Zn co-doped complex perovskite $\text{CaCu}_3\text{Ti}_4\text{O}_{12}$ ceramic, *Ceram. Int.* 44 (2018) 23125–23136. <https://doi.org/10.1016/j.ceramint.2018.09.121>.
- [18] S. Chung, I. Kim, S.L. Kang, Strong nonlinear current–voltage behaviour in perovskite-derivative calcium copper titanate, *Nat. Mater.* 3 (2004) 774–778. <https://doi.org/10.1038/nmat1238>.
- [19] J. Boonlakhorn, P. Thongbai, Effect of Annealing in O_2 and Mechanisms Contributing to the Overall Loss Tangent of $\text{CaCu}_3\text{Ti}_4\text{O}_{12}$ Ceramics, *J. Electron. Mater.* 44 (2015) 3687–3695. <https://doi.org/10.1007/s11664-015-3888-0>.
- [20] J. Liu, Q. Liu, W. Wang, Y. Liang, D. Lu, P. Zhu, Variable-range-hopping conduction

- and polaron dielectric relaxation in Cu and Nb co-doped BaTiO₃, *J. Phys. Chem. Solids*. 129 (2019) 111–121. <https://doi.org/10.1016/j.jpcs.2018.12.036>.
- [21] P. Mao, J. Wang, S. Liu, L. Zhang, Y. Zhao, L. He, Grain size effect on the dielectric and non-ohmic properties of CaCu₃Ti₄O₁₂ ceramics prepared by the sol-gel process, *J. Alloys Compd.* 778 (2019) 625–632. <https://doi.org/10.1016/j.jallcom.2018.11.200>.
- [22] B.S. Prakash, K.B.R. Varma, Molten salt synthesis of nanocrystalline phase of high dielectric constant material CaCu₃Ti₄O₁₂, *J. Nanosci. Nanotechnol.* 8 (2008) 5762–5769. <https://doi.org/10.1166/jnn.2008.213>.
- [23] P. Lunkenheimer, S. Krohns, S. Riegg, S.G. Ebbinghaus, A. Reller, A. Loidl, Colossal dielectric constants in transition-metal oxides, *Eur. Phys. J. Spec. Top.* 180 (2009) 61–89. <https://doi.org/10.1140/epjst/e2010-01212-5>.
- [24] C.C. Homes, T. Vogt, S.M. Shapiro, S. Wakimoto, A.P. Ramirez, Optical Response of Perovskite-Related Oxide, 293 (2001) 673–677.
- [25] P. Lunkenheimer, V. Bobnar, V. Bobnar, A. V. Pronin, A. V. Pronin, A.I. Ritus, A.A. Volkov, A. Loidl, Origin of apparent colossal dielectric constants, *Phys. Rev. B - Condens. Matter Mater. Phys.* 66 (2002) 521051–521054. <https://doi.org/10.1103/PhysRevB.66.052105>.
- [26] A.K. Thomas, K. Abraham, J. Thomas, K.V. Saban, Electrical and dielectric behaviour of Na_{0.5}La_{0.25}Sm_{0.25}Cu₃Ti₄O₁₂ ceramics investigated by impedance and modulus spectroscopy, *J. Asian Ceram. Soc.* 5 (2017) 56–61. <https://doi.org/10.1016/j.jascer.2017.01.002>.
- [27] M.A. Subramanian, D. Li, N. Duan, B.A. Reisner, A.W. Sleight, High Dielectric Constant in ACu₃Ti₄O₁₂ and ACu₃Ti₃FeO₁₂ Phases, *J. Solid State Chem.* 151 (2000) 323–325. <https://doi.org/10.1006/jssc.2000.8703>.

- [28] A.K. Thomas, K. Abraham, J. Thomas, K.V. Saban, Electrical and dielectric behaviour of $\text{Na}_{0.5}\text{La}_{0.25}\text{Sm}_{0.25}\text{Cu}_3\text{Ti}_4\text{O}_{12}$ ceramics investigated by impedance and modulus spectroscopy, *J. Asian Ceram. Soc.* 5 (2017) 56–61. <https://doi.org/10.1016/j.jascer.2017.01.002>.
- [29] S. Vangchangyia, E. Swatsitang, P. Thongbai, S. Pinitsoontorn, T. Yamwong, S. Maensiri, V. Amornkitbamrung, P. Chindaprasirt, Very Low Loss Tangent and High Dielectric Permittivity in Pure- $\text{CaCu}_3\text{Ti}_4\text{O}_{12}$ Ceramics Prepared by a Modified Sol-Gel Process, *J. Am. Ceram. Soc.* 95 (2012) 1497–1500. <https://doi.org/10.1111/j.1551-2916.2012.05147.x>.
- [30] M.A.L. Nobre, S. Lanfredi, Dielectric loss and phase transition of sodium potassium niobate ceramic investigated by impedance spectroscopy, *Catal. Today.* 78 (2003) 529–538. [https://doi.org/10.1016/S0920-5861\(02\)00349-8](https://doi.org/10.1016/S0920-5861(02)00349-8).
- [31] P. Lunkenheimer, S. Krohns, S. Riegg, S.G. Ebbinghaus, A. Reller, A. Loidl, Colossal dielectric constants in transition-metal oxides, *Eur. Phys. J. Spec. Top.* 180 (2009) 61–89. <https://doi.org/10.1140/epjst/e2010-01212-5>.
- [32] P. Fiorenza, R. Lo Nigro, C. Bongiorno, V. Raineri, M.C. Ferarrelli, D.C. Sinclair, A.R. West, Localized electrical characterization of the giant permittivity effect in $\text{CaCu}_3\text{Ti}_4\text{O}_{12}$ ceramics, *Appl. Phys. Lett.* 92 (2008) 182907. <https://doi.org/10.1063/1.2919095>.
- [33] K. Kumar, K.K. Kar, R. Janakarajan, *Journal of Physics and Chemistry of Solids* Enhanced microwave sintering characteristics , electrical and thermal properties of nano Li_2TiO_3 ceramic and its nanocomposite using $\text{LiNi}_{0.5}\text{Co}_{0.5}\text{PO}_4$ as high-capacity cathode for Li-ion batteries, *J. Phys. Chem. Solids.* 135 (2019) 109099. <https://doi.org/10.1016/j.jpcs.2019.109099>.

- [34] L. Zhang, Z. Tang, Polaron relaxation and variable-range-hopping conductivity in the giant-dielectric-constant material $\text{CaCu}_3\text{Ti}_4\text{O}_{12}$, *Phys. Rev. B.* 70 (2004) 174306. <https://doi.org/10.1103/PhysRevB.70.174306>.
- [35] A.K. Jonscher, Dielectric relaxation in solids, *J. Phys. D. Appl. Phys.* 32 (1999). <https://doi.org/10.1088/0022-3727/32/14/201>.
- [36] D.K. Pradhan, B. Behera, P.R. Das, Studies of dielectric and electrical properties of a new type of complex tungsten bronze electroceramics, *J. Mater. Sci. Mater. Electron.* 23 (2012) 779–785. <https://doi.org/10.1007/s10854-011-0492-9>.
- [37] T. Badapanda, V. Senthil, S.K. Rout, L.S. Cavalcante, A.Z. Simões, T.P. Sinha, S. Panigrahi, M.M. De Jesus, E. Longo, J.A. Varela, Rietveld refinement, microstructure, conductivity and impedance properties of $\text{Ba}[\text{Zr}_{0.25}\text{Ti}_{0.75}]\text{O}_3$ ceramic, *Curr. Appl. Phys.* 11 (2011) 1282–1293. <https://doi.org/10.1016/j.cap.2011.03.056>.
- [38] D. ALMOND, G. DUNCAN, A. WEST, The determination of hopping rates and carrier concentrations in ionic conductors by a new analysis of ac conductivity, *Solid State Ionics.* 8 (1983) 159–164. [https://doi.org/10.1016/0167-2738\(83\)90079-6](https://doi.org/10.1016/0167-2738(83)90079-6).
- [39] M.K.H. Bhuiyan, M.A. Gafur, M.N.I. Khan, A.A. Momin, A.K.M.A. Hossain, Correlations of Structural, Dielectric, Magnetic and Magnetoelectric Properties of $\text{Ca}_{1-x}\text{Sr}_x(\text{Fe}_{1-y}\text{Nb}_y\text{Ta}_{0.5})$, *Mater. Sci. Appl.* 08 (2017) 64–84. <https://doi.org/10.4236/msa.2017.81005>.
- [40] A.. Jonscher, © 1977 Nature Publishing Group, *Nature.* 267 (1977) 673–679.
- [41] S. Singh, P.A. Jha, S. Varma, P. Singh, Large polaron hopping phenomenon in lanthanum doped strontium titanate, *J. Alloys Compd.* 704 (2017) 707–716.

<https://doi.org/10.1016/j.jallcom.2017.02.015>.

- [42] L. He, J.B. Neaton, D. Vanderbilt, M.H. Cohen, Lattice dielectric response of CdCu_3Ti_4 , Phys. Rev. B. 67 (2003) 012103.

<https://doi.org/10.1103/PhysRevB.67.012103>.

- [43] E. Veena Gopalan, K.A. Malini, S. Saravanan, D. Sakthi Kumar, Y. Yoshida, M.R. Anantharaman, Evidence for polaron conduction in nanostructured manganese ferrite, J. Phys. D. Appl. Phys. 41 (2008) 185005. <https://doi.org/10.1088/0022-3727/41/18/185005>.

- [44] A.R. West, T.B. Adams, F.D. Morrison, D.C. Sinclair, Novel high capacitance materials:- BaTiO₃:La and CaCu₃Ti₄O₁₂, J. Eur. Ceram. Soc. 24 (2004) 1439–1448. [https://doi.org/10.1016/S0955-2219\(03\)00510-7](https://doi.org/10.1016/S0955-2219(03)00510-7).

- [45] S. Pandey, D. Kumar, O. Parkash, L. Pandey, Equivalent circuit models using CPE for impedance spectroscopy of electronic ceramics, Integr. Ferroelectr. 183 (2017) 141–162. <https://doi.org/10.1080/10584587.2017.1376984>.

- [46] S. Pandey, D. Kumar, O. Parkash, L. Pandey, Impedance Spectroscopy: A Powerful Technique for Study of Electronic Ceramics, in: Ceram. Mater. - Synth. Charact. Appl. Recycl., IntechOpen, 2019. <https://doi.org/10.5772/intechopen.81398>.

- [47] W. Reitz, A Review of: “ Impedance Spectroscopy, Theory, Experiment, and Applications , E. Barsoukov and J. R. Macdonald, (editors).,” Mater. Manuf. Process. 22 (2007) 294–294. <https://doi.org/10.1080/10426910601067395>.

- [48] J.R. Macdonald, Impedance spectroscopy: old problems and new developments,

- Electrochim. Acta. 35 (1990) 1483–1492. [https://doi.org/10.1016/0013-4686\(90\)80002-6](https://doi.org/10.1016/0013-4686(90)80002-6).
- [49] S.K. Barik, R.N.P. Choudhary, P.K. Mahapatra, Impedance spectroscopy study of Na_{1/2}Sm_{1/2}TiO₃ ceramic, Appl. Phys. A. 88 (2007) 217–222. <https://doi.org/10.1007/s00339-007-3990-0>.
- [50] J. Shanker, M.B. Suresh, D.S. Babu, Synthesis, Characterization and Impedance Spectroscopy Studies of NdFeO₃ Perovskite Ceramics, Int. J. Sci. Eng. Res. 3 (2015) 3–7.
- [51] K.S. Cole, R.H. Cole, Dispersion and Absorption in Dielectrics I. Alternating Current Characteristics, J. Chem. Phys. 9 (1941) 341–351. <https://doi.org/10.1063/1.1750906>.
- [52] N. V. Prasad, M.C. Sekhar, G.S. Kumar, Impedance Spectroscopic Studies on Lead Based Perovskite Materials, Ferroelectrics. 366 (2008) 55–66. <https://doi.org/10.1080/00150190802363140>.
- [53] R. Gerhardt, Impedance and dielectric spectroscopy revisited: Distinguishing localized relaxation from long-range conductivity, J. Phys. Chem. Solids. 55 (1994) 1491–1506. [https://doi.org/10.1016/0022-3697\(94\)90575-4](https://doi.org/10.1016/0022-3697(94)90575-4).

Figures

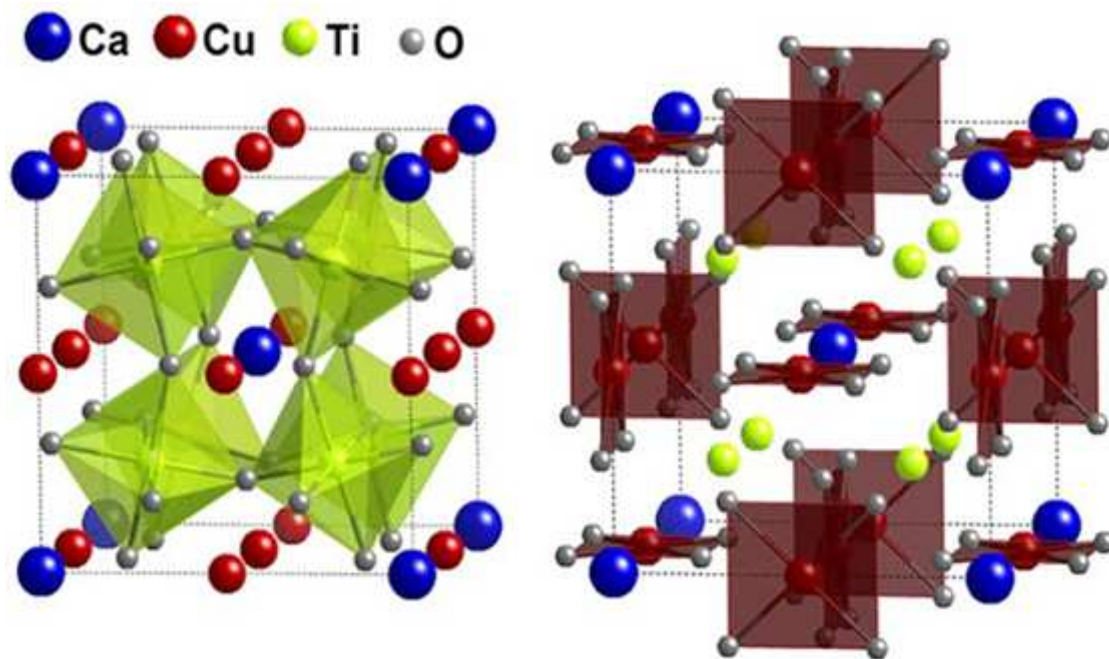


Figure 1

See the Manuscript Files section for the complete figure caption.

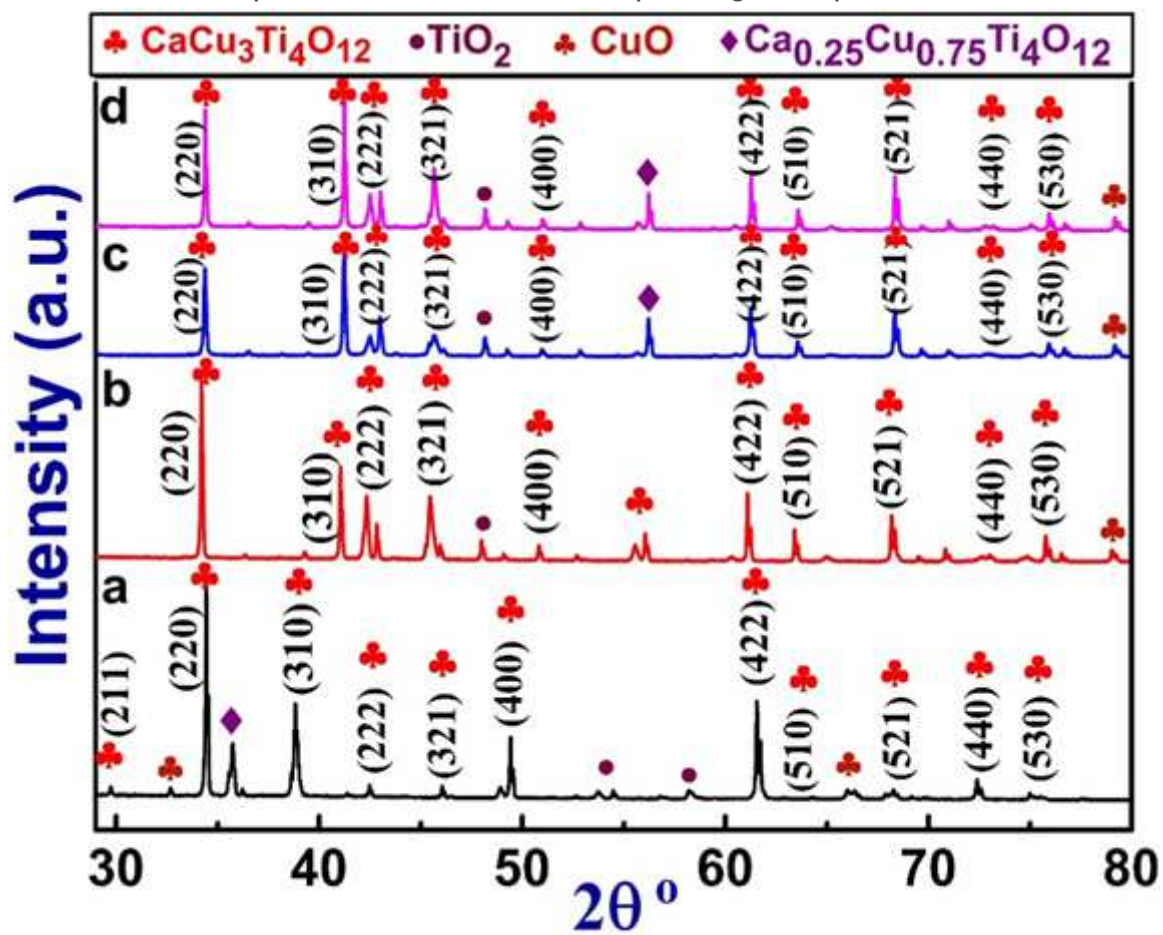


Figure 2

See the Manuscript Files section for the complete figure caption.

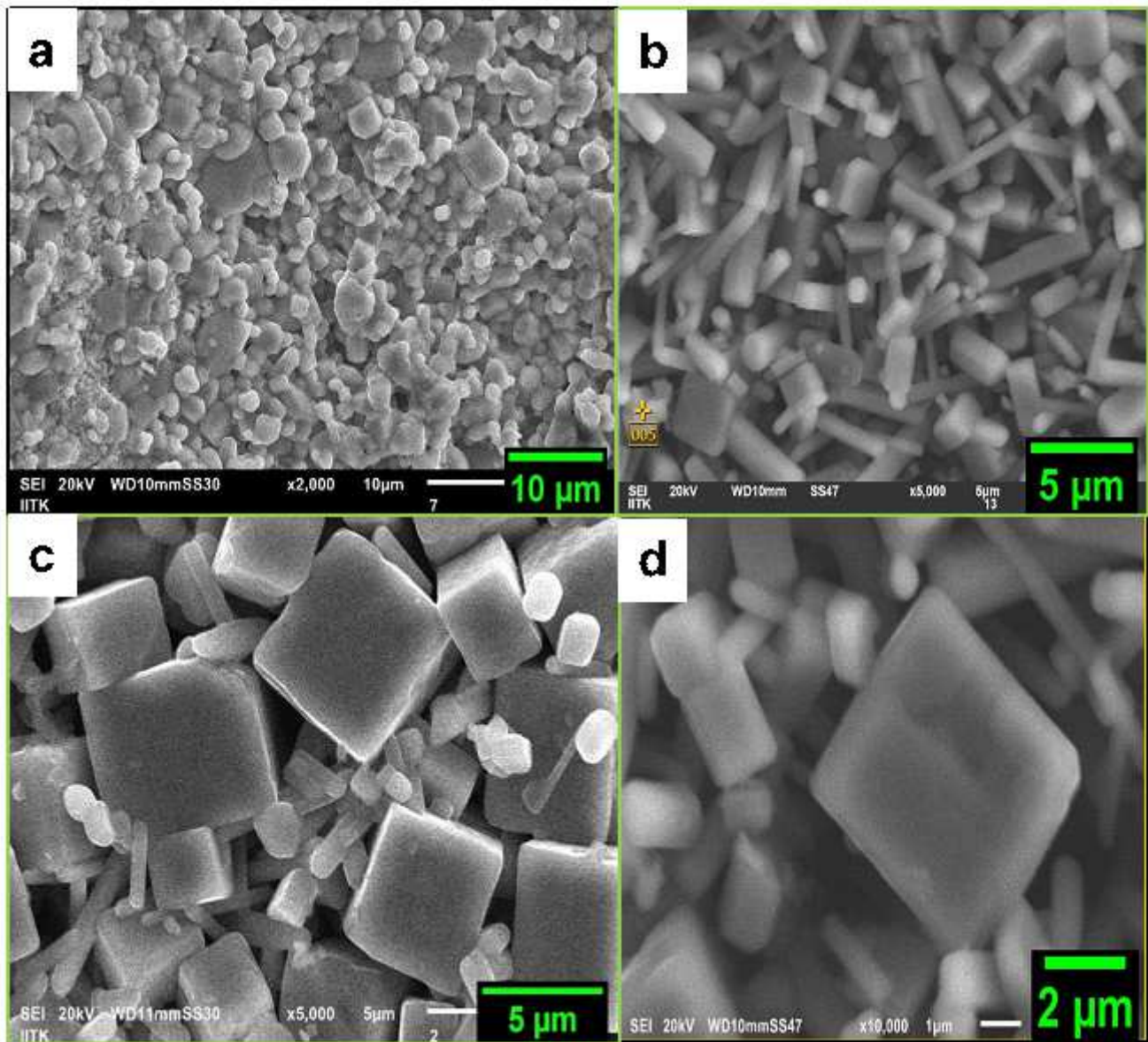


Figure 3

See the Manuscript Files section for the complete figure caption.

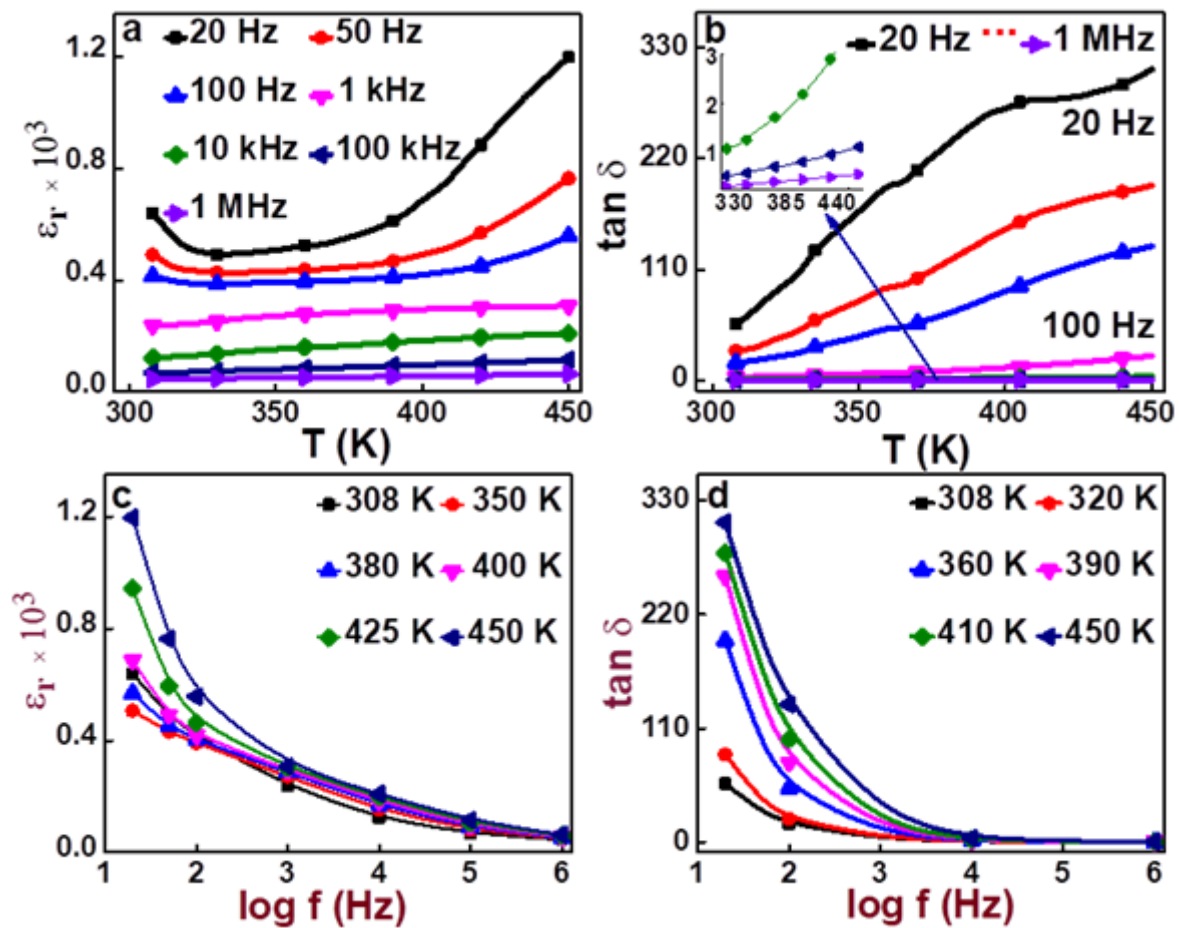


Figure 4

See the Manuscript Files section for the complete figure caption.

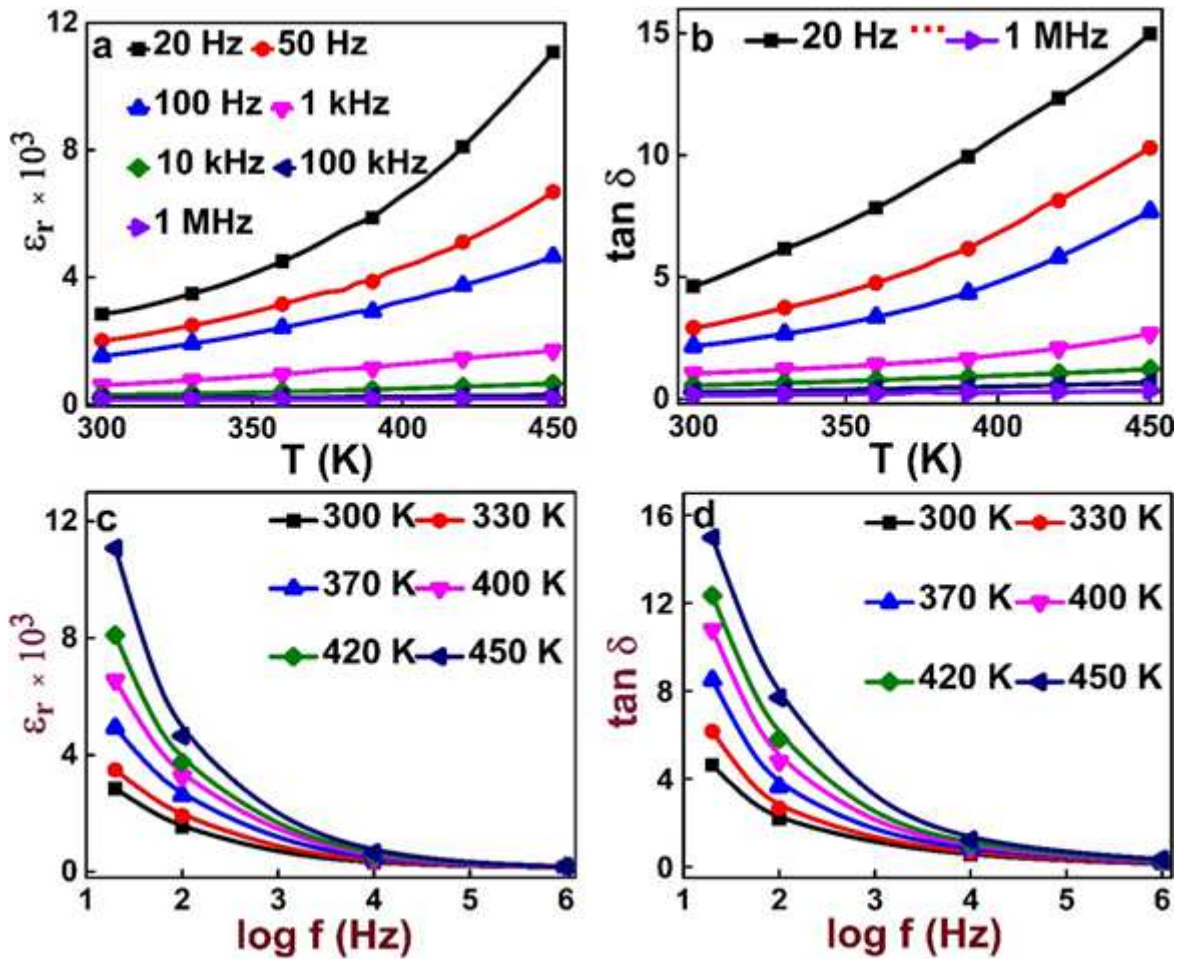


Figure 5

See the Manuscript Files section for the complete figure caption.

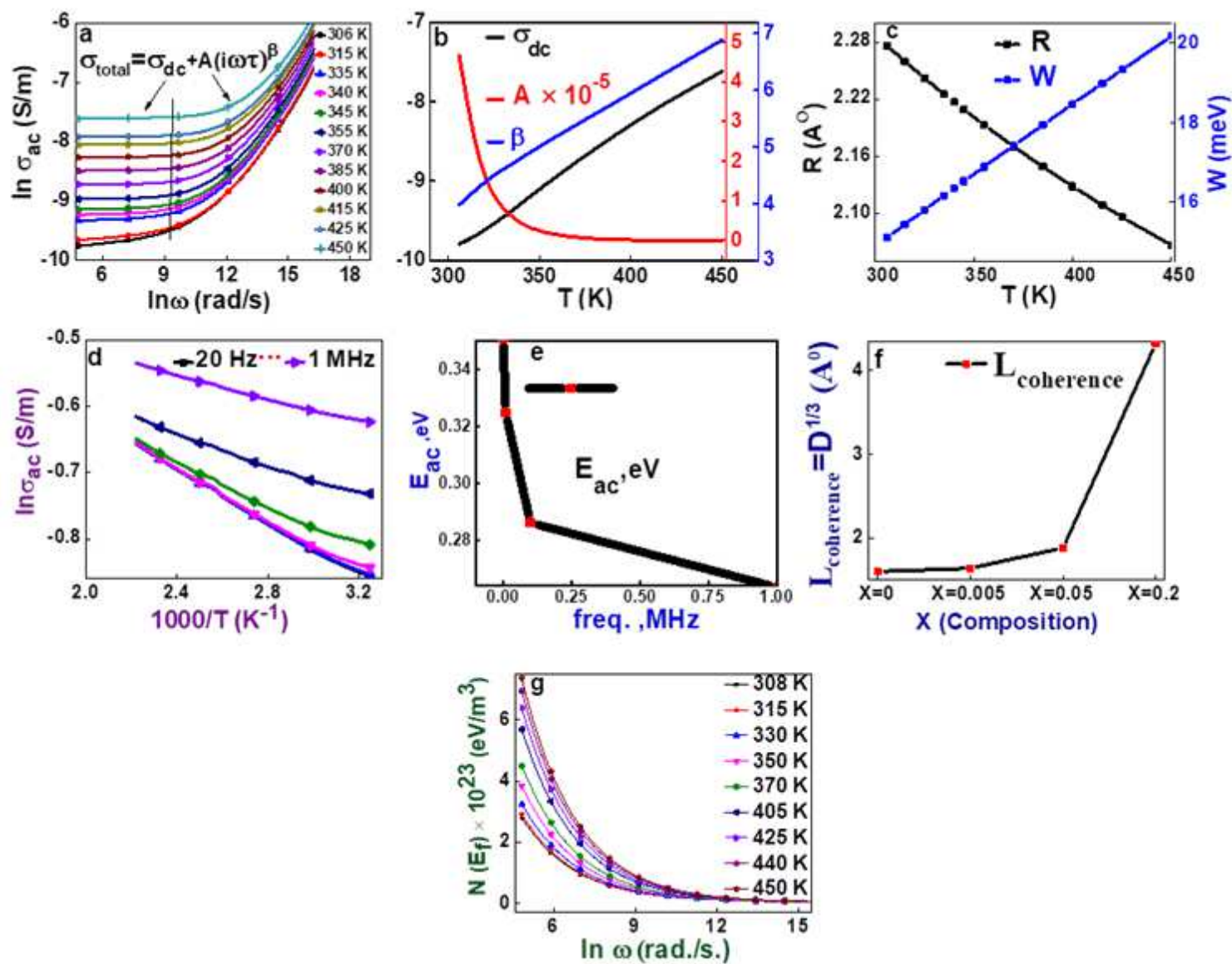


Figure 6

See the Manuscript Files section for the complete figure caption.

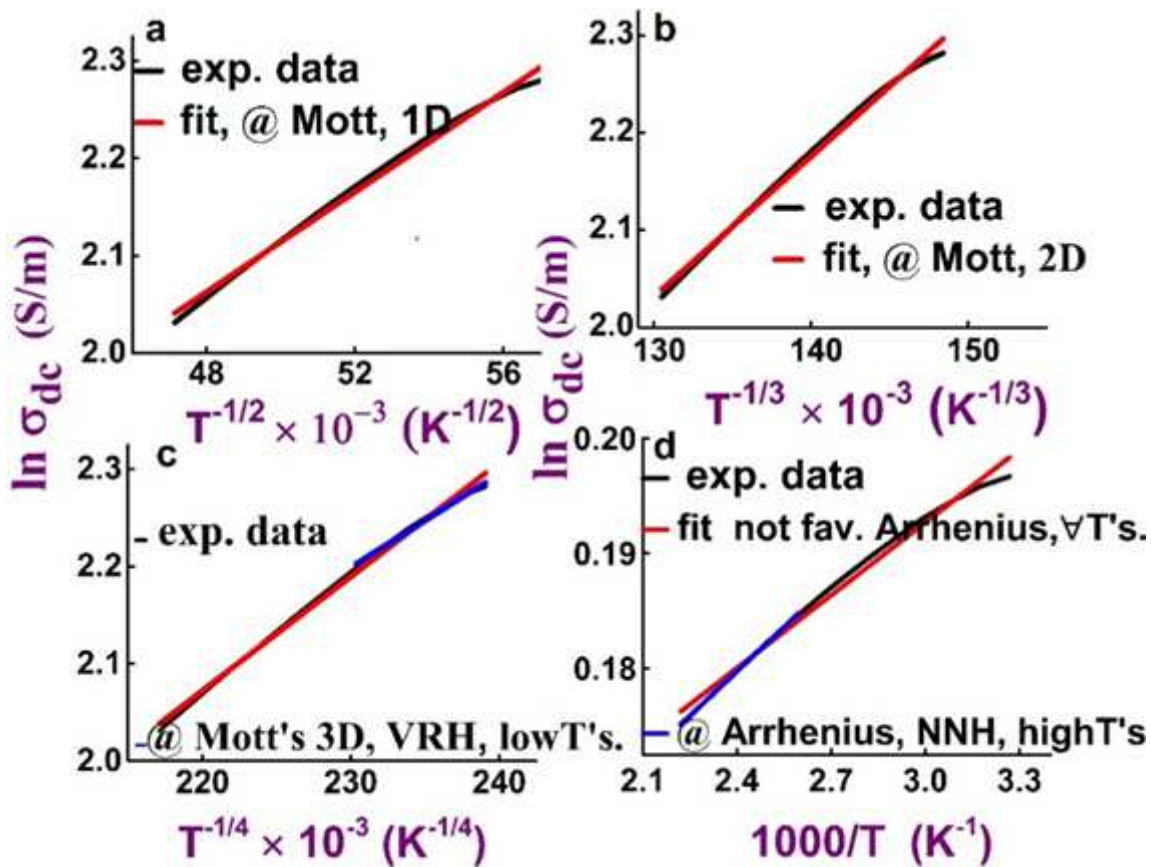


Figure 7

See the Manuscript Files section for the complete figure caption.

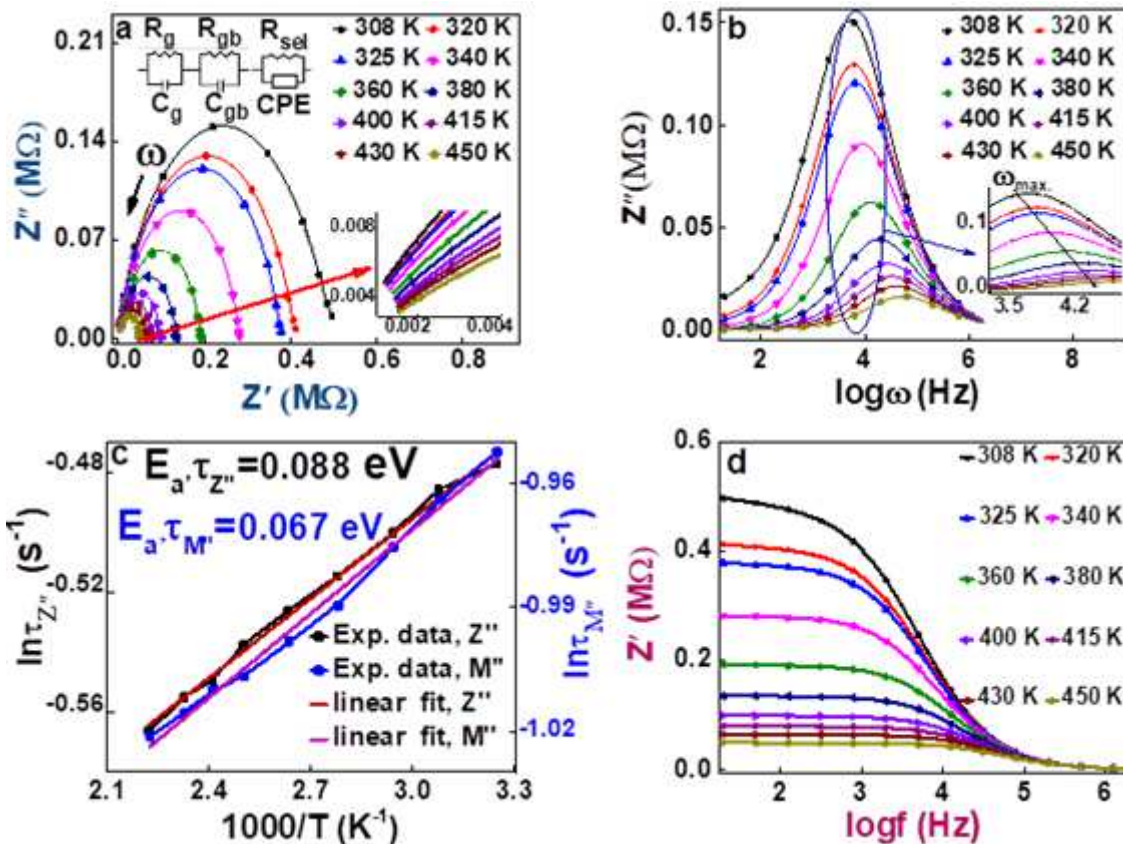


Figure 8

See the Manuscript Files section for the complete figure caption.

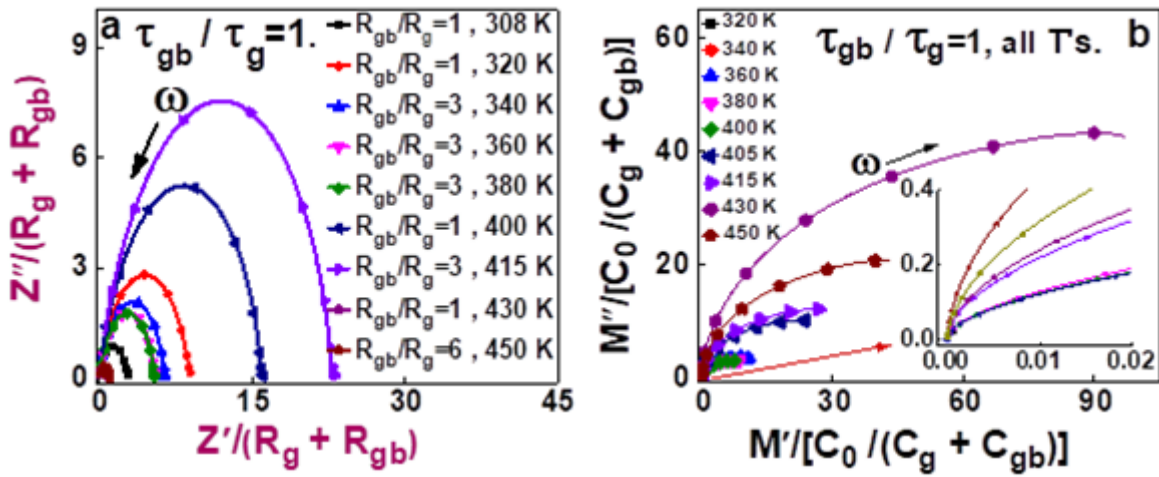


Figure 9

See the Manuscript Files section for the complete figure caption.

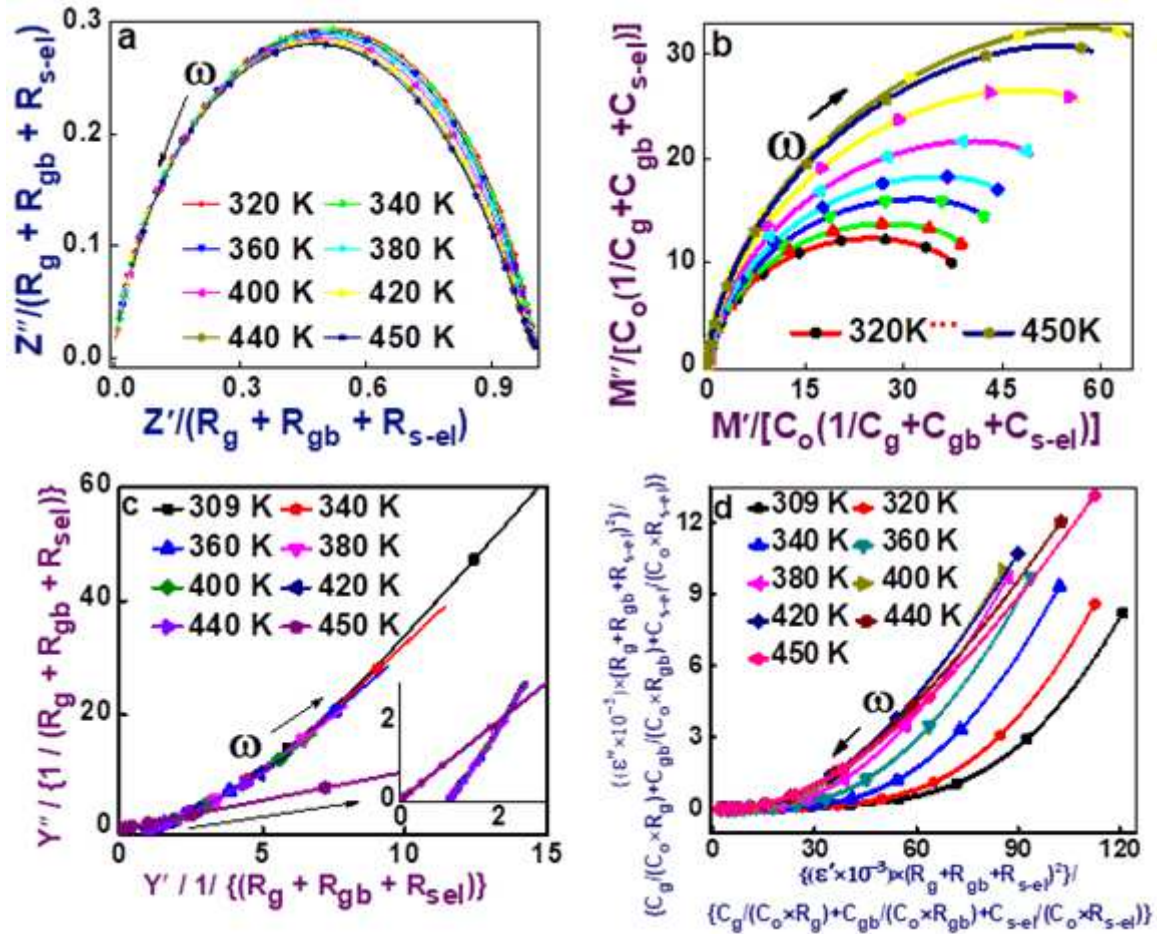


Figure 10

See the Manuscript Files section for the complete figure caption.

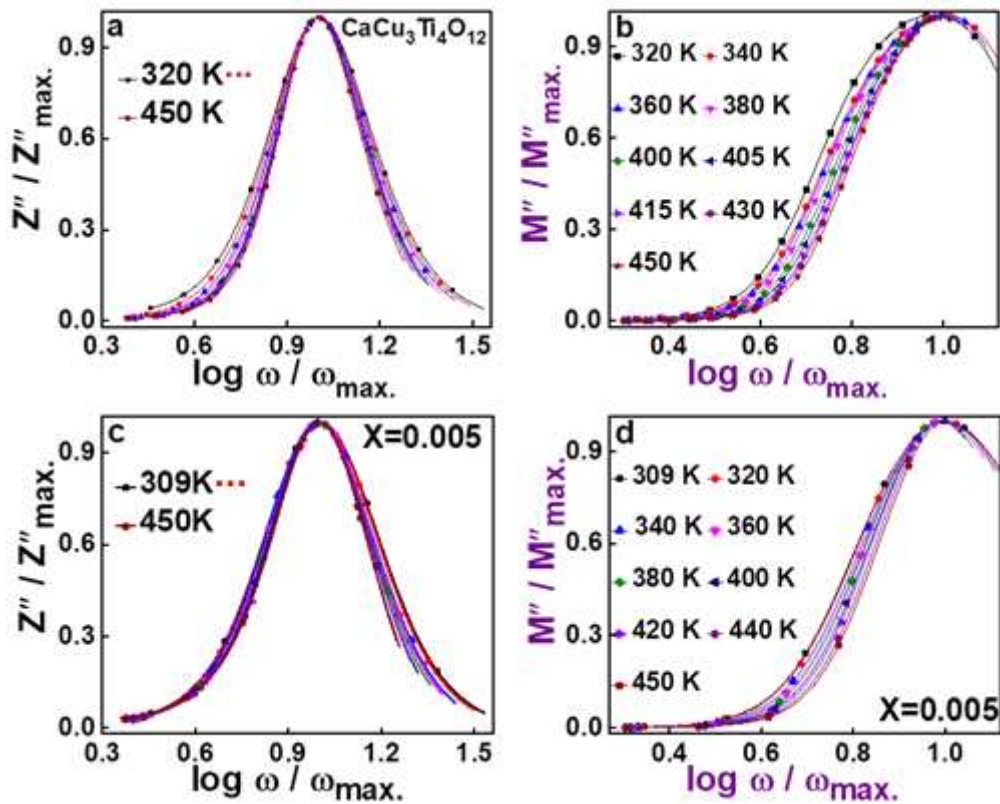


Figure 11

See the Manuscript Files section for the complete figure caption.

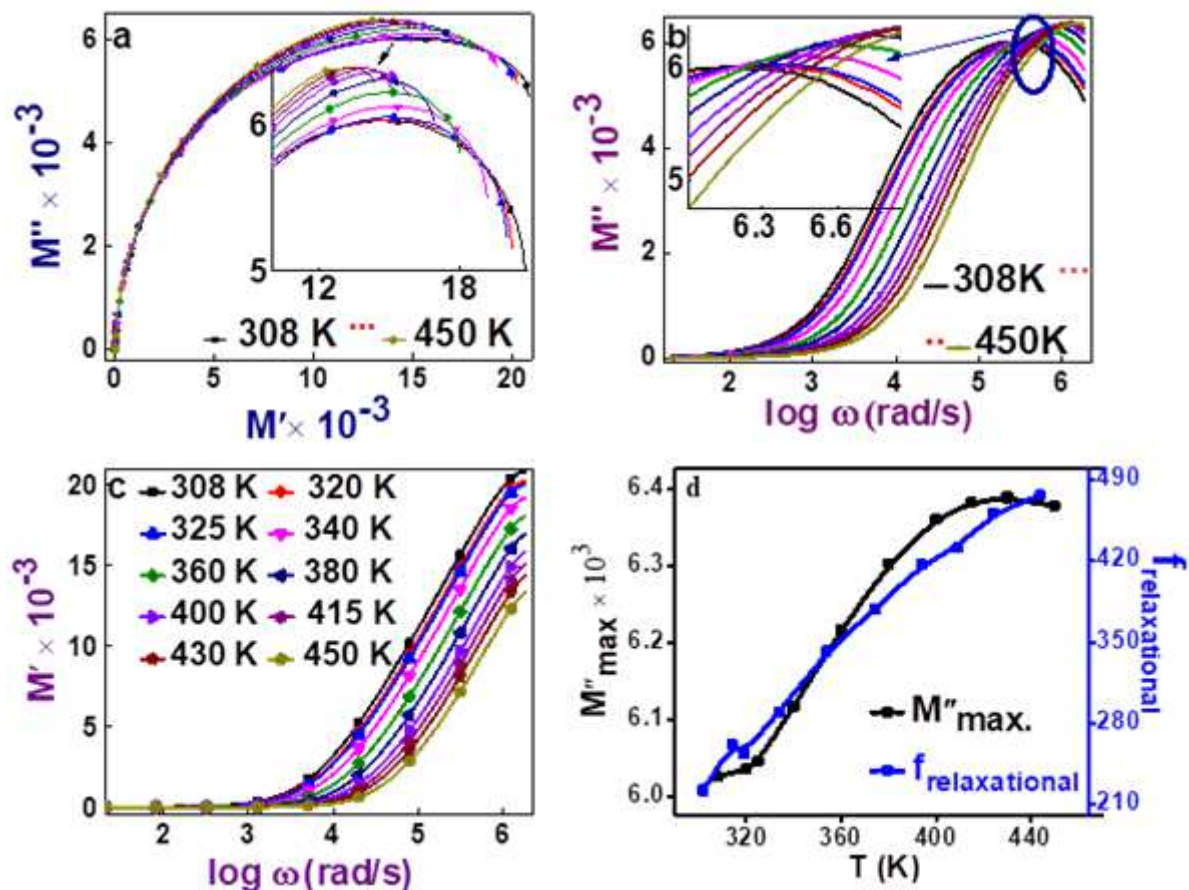


Figure 12

See the Manuscript Files section for the complete figure caption.

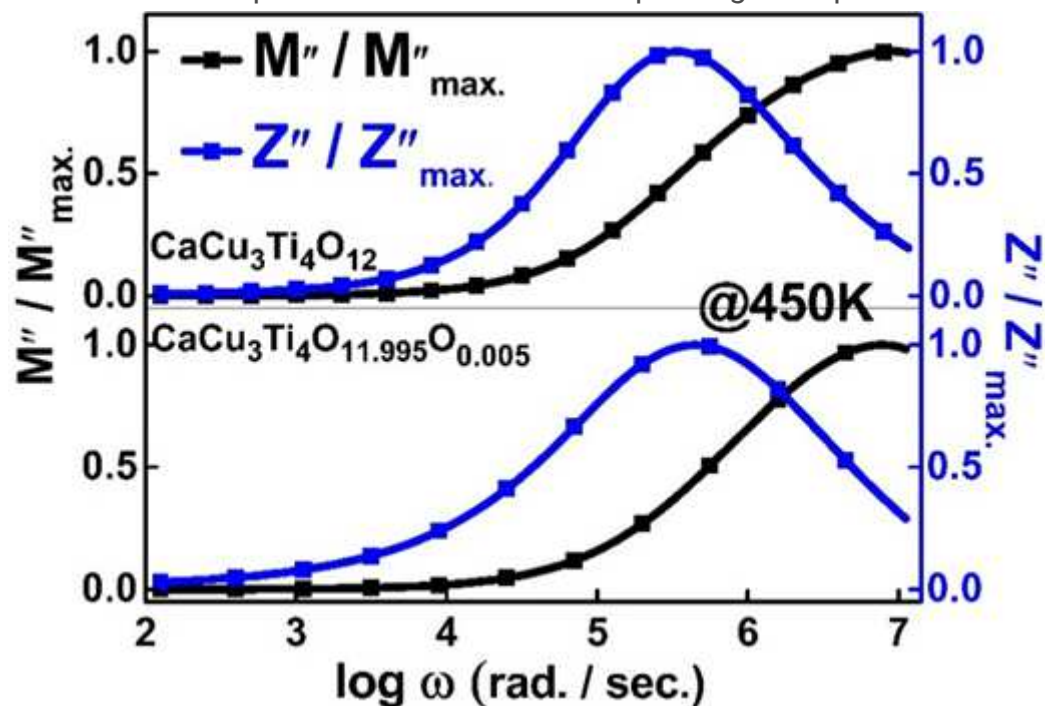


Figure 13

See the Manuscript Files section for the complete figure caption.

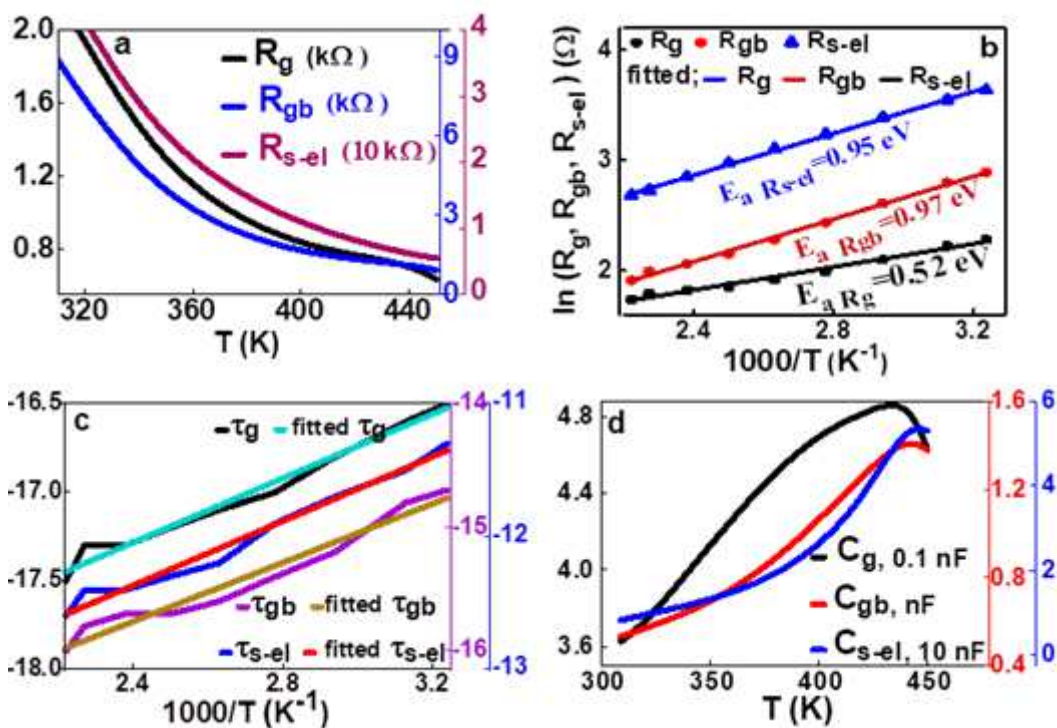


Figure 14

See the Manuscript Files section for the complete figure caption.